Article

Enabling Power System Restoration from Offshore Wind Power Plants in the UK

Rui Alves *, Ning Yang, Lie Xu and Agustí Egea-Àlvarez

Department of Electronic and Electrical Engineering, University of Strathclyde, 16 Richmond St, Glasgow G1 1XQ, UK; ning.yang@strath.ac.uk (N.Y.); lie.xu@strath.ac.uk (L.X.); agusti.egea@strath.ac.uk (A.E.-À.)
* Correspondence: rui.do-amaral-alves@strath.ac.uk

Abstract: This paper presents the findings from the initial phases of the SIF BLADE project, focused on demonstrating the capabilities of an offshore wind power plant (OWPP) for power system restoration (PSR). It provides an overview of PSR, highlighting its challenges and operational requirements, alongside the various scenarios considered in the project. The study includes a steady-state analysis to assess whether the OWPP can meet local network demands for both active and reactive power. Results indicate that the OWPP can operate within an envelope that covers all local power requirements. Additionally, electromagnetic transient (EMT) analysis was conducted to evaluate different percentages of grid-forming (GFM) converter penetration during the energisation process. These analyses aimed to determine compliance with transmission system operator (TSO) requirements. Findings demonstrate that all GFM penetration levels met the necessary TSO standards. Furthermore, a novel small-signal analysis was performed to identify the optimal percentage of GFM converters for enhancing system stability during block loading. The analysis suggests that for top-up scenarios, a GFM penetration between 20% and 40% is optimal, while for anchor scenarios, 40% to 60% GFM penetration enhances stability and robustness.

Keywords: black start; converter control; EMT analysis; grid-following; grid-forming; power system restoration; small-signal analysis; stability

1. Introduction

Wind energy is becoming a prominent player in the global energy mix, and this trend is expected to continue. One of the main drivers is the need for decarbonization to achieve carbon neutrality, as stipulated in the Paris Agreement of 2015. The European Union aims for 32% of its electricity mix to come from renewable energy sources (RESs) by 2030. As of 2020, this percentage was 19.7%, with 16.9% of this electricity produced by wind turbines (WTs) [1]. In the UK, 24.8% of the electricity mix came from wind energy, with 11% generated by offshore wind power plants (OWPPs) [2]. This unprecedented change in the electrical system has resulted from the decommissioning of fossil fuel-based generators and their replacement with inverter-based RESs.

With the increasing integration of converter-connected RESs into power grids, it is essential to ensure the resilience of power systems in the event of partial or total blackouts. Recent geopolitical tensions, such as those in Ukraine, Syria, and Israel, have further emphasised the increasing likelihood of disruptions to critical infrastructure, including power grids, through cyber-attacks and physical threats. Traditionally, the responsibility for restoring power, known as power system restoration (PSR) or black start (BS), has rested with a few large, transmission-connected synchronous generating power stations.

However, as these stations are phased out, the task of providing restoration services must also transition accordingly, and thus RESs such as OWPPs, photovoltaics (PVs), and battery energy storage systems (BESSs) should also be considered as black start units (BSUs) [3,4]. BSUs are generation assets capable of restarting without support from the electrical grid. In particular, PSR using wind power has not previously been seen as a priority, but due to the high number of planned OWPPs, 50 GW by 2030 [5], it is a matter of energy security to consider this option for the future of PSR in the UK.

Having this in mind, several projects emerged in the UK and European Union aiming at research involving both industry and academia in which it was investigated if RESs can potentially contribute to the UK's PSR in case of a blackout. An example is the PROMO-TioN project, which focused on developing meshed HVDC offshore grids, investigated OWPP/WT control for self-start and BS [6,7]; another is Distributed ReStart, which explored how distributed energy resources (DERs) such as solar, wind, and hydro, may be used for PSR [8].

Following this trend, the project SIF BLADE [9] was launched, aiming to explore and demonstrate how innovative, cost-effective, low-carbon technologies can enable OWPPs to restore the onshore grid following a blackout. Validating this concept will facilitate the accelerated deployment of OWPPs to replace existing fossil fuel generators while mitigating any potential resilience challenges that may arise. OWPPs have emerged as a critical component of RESs, offering stronger and more consistent wind resources compared to onshore installations and thus being a strong candidate to provide black start services. As these farms are developed farther from shore, challenges related to stability, transmission and grid support become increasingly significant, especially during scenarios such as power system restoration.

Offshore wind farms typically employ one of two main types of wind turbine generators: Doubly-Fed Induction Generators (DFIGs) and Permanent Magnet Synchronous Generators (PMSGs). DFIGs, with their partially rated converters, are widely used due to their cost efficiency and established technology. However, their limited capability for grid support under extreme conditions can pose challenges in scenarios requiring high levels of control flexibility. PMSGs, on the other hand, feature fully rated converters, enabling superior grid-forming capabilities, which are essential for advanced applications like power system restoration. This study focuses on the use of an aggregated wind farm model consisting of PMSG-based wind turbines to evaluate their potential in restoring power systems. By leveraging their full converter design, the analysis provides insights into stability and reliability in offshore wind farms connected via HVAC transmission systems.

This paper aims to present the key topics discussed and analysed during the initial stages of the SIF BLADE project: the Discovery Phase and the Alpha Phase. Below, the studies conducted during these phases are detailed, along with the sections where each topic is discussed.

Section 2 presents various studies conducted during the Discovery Phase of the SIF BLADE Project. These studies included an overview of the PSR process. PSR requirements and challenges are examined in the context of OWPPs, and an investigation is conducted into possible scenarios involving the location of the auxiliary power supply (APS) unit responsible for starting up the OWPP and the need for self-start, grid forming (GFM) WTs.

Sections 3–6 present results from the Alpha Phase of the SIF BLADE project. Section 3 introduces the hardware model and converter control strategies used in the study. The hardware model was designed taking into account information from several partners of the SIF BLADE project, as well as a benchmark OWPP suggested in the CIGRE documentation. With regards to converter control strategies, two were used, a grid following (GFL) one and a GFM one.

Section 4 examines whether the designed OWPP and power system could meet, in steady state, local network demand in terms of active and reactive power operating points, using data from a project partner. This was performed via power flow analysis after developing an impedance model and its Thevenin equivalent.

The next two studies examine the need for, and benefits of, including GFM converter controllers in the PSR process. These studies were performed for both "anchor" and "top-up" generation possibilities. These two terms have been added to the Grid Code legal text (GC0156) to clarify the roles of different parties involved in restoration services, based on how actively they participate in the restoration process [10]. The anchor generation assumes the role of system energisation, effectively having an active role in rebuilding the skeleton network and block loading, whereas the top-up generation scenario only accounts for its block loading capabilities, hence just providing active and reactive power as required.

Section 5 delves into electromagnetic transient (EMT) simulations, while Section 6 focuses on linear time-invariant (LTI) studies via small-signal model (SSM). The EMT analysis aimed to analyse if there is an optimal percentage of GFM penetration to meet transmission system operator (TSO) requirements, mitigate potential challenges, and maintain stable operation during PSR. The novelty of this research lies in the LTI studies, which involved a stability analysis via SSM—a study not yet performed in the context of PSR. This study aimed to determine the best percentage of GFM penetration for enhanced stability and robustness of the power system in scenarios involving anchor and top-up generation during block loading.

2. Power System Restoration from Offshore Wind Power Plants—An Overview

PSR is a complex process with low probability but high impact [11]. This section provides an overview of the PSR process, highlighting its challenges identified by both academia and industry. Additionally, the requirements for PSR are discussed. Finally, the section presents the scenarios studied in this project concerning the location of the auxiliary power supply that will provide the energy required to start-up the OWPP.

2.1. PSR Process

PSR is the ability to restore a power system to its normal state after a partial or total blackout, ideally with minimum losses and restoration time, thereby minimizing economic and social impacts [12]. Traditionally speaking, the stages of power system restoration are split into three different areas, which are BS, network reconfiguration, and load restoration [13–15].

The BS stage is characterised by a BSU providing cranking power to a non-black-start unit (NBSU), hence energising units that are not self-start-capable [15]. This phase also involves identifying the affected power system, including the location of critical loads, the status of circuit breakers, and the availability and location of the BSU [3,16,17]. Entities such as the TSO will then choose the BSU to restart the system, considering factors such as cost reduction, restoration time, and paths. In the case of OWPPs, if there are multiple BSUs and wind forecasts are favorable, different units will contribute to system restoration; thus, the system is split into generating islands that will later be synchronized [1,2,15].

After a BSU establishes an energised path and supplies the cranking power to an NBSU, the generation capacity increases. The focus of network reconfiguration is on restoring additional generators, constructing the skeleton network that includes key substations and branches, and preparing the system for the final stage of PSR. To accomplish this, the network reconfiguration stage must follow an optimized restoration procedure to ensure a successful restoration and minimize the risk of system re-collapse. According to [3–5,13],

this procedure includes enhancing the grid resilience by including temporary backup power, emergency power supplies, topology reconfiguration, substation relocation and transmission line rerouting.

During the BS phase, a BSU unit is employed to energise the electrical path and supply power to an NBSU. This stage focuses on restoring enough load to enable the BSU unit to achieve its minimum operational output. As the process transitions to the network reconfiguration stage, increased generation capacity allows for the restoration of additional loads, helping to balance the load and generation levels [14]. This stage also provides the opportunity to restore critical loads. Prior to the third stage, load pickup primarily serves to manage system frequency. In contrast, the third stage is dedicated to restore as quickly as possible the rest of the loads connected in the system [17,18].

AThe aforementioned is the traditional set up for PSR. Nevertheless, this approach may also be followed if considering system restoration from RESs, more specifically, from OWPPs. However, due to the new technologies implemented in OWPPs such as inverter-based generators, some challenges and concerns will be distinct.

OWPPs have the potential to provide PSR due to their large capacity and the increasing sophistication of their technology. The process begins with the self-start capability of the OWPP, which can be facilitated by cranking the WT via an external power supply such as a BESS or GFM WT. It should be mentioned, however, that the GFM technology is new and thus immature and presents several technology complexities. Furthermore, GFM WTs may come with extra costs that should be considered. These systems can establish an initial power island by energising part of the OWPP independently of the main transmission network [19]. Once the initial power island is established, the OWPP can progressively energise larger sections of the grid through a method known as block loading. This involves sequentially connecting and energising sections of the transmission network until the entire system is fully restored. During this phase, the OWPP must maintain voltage and frequency control to ensure stability and prevent overloading [20]. A critical aspect of the restoration process is the synchronization of the OWPP with other energised sections of the grid. This requires control and coordination to match the phase and frequency of the local grid with the larger transmission network [20,21]. Once synchronized, the OWPP can contribute to the overall stability and resiliency of the power system, providing a renewable-based alternative to conventional black start sources.

2.2. Challenges and Requirements of PSR from OWPPs

The European Network of Transmission System Operators (ENTSO-E) included BS and island operation as optional requirements for connected AC and HVDC OWPPs. However, there are currently no PSR requirements specifically dedicated for OWPPs [20]. However, several TSOs, such as Elia from Belgium and National Grid ESO (NGESO) from the United Kingdom, have proposed a set of requirements [8,10,22]. This section describes succinctly some of those requirements that shall be used later in Section 5 for the EMT studies. It also dives into challenges identified for PSR from OWPPs. For further details on all the requirements, readers are encouraged to consult references [8,10,20–22] as several requirements such as trip to household, time to connect, and service availability are not considered in this study.

2.2.1. Self-Start Capability

A BSU needs to be able to self-start without any external power supply within a specific time frame which is dependent on the TSO. Traditional WTs are not self-start-capable as they are GFL units and thus follow a voltage reference signal from another voltage source. However, GFM units, if allied with an APS such as an internal BESS

or an external APS available to provided cranking power, are able to sustain a voltage reference signal and are thus self-start-capable.

2.2.2. Block Loading Capability

Block loading capability refers to a BSU's ability to accept an instantaneous block load. For the NGESO, as noted in [8], the preferred range for this value is between 35 and 50 MW while maintaining voltage and frequency within acceptable limits. The NGESO specifies that block loading should be determined by the voltage level at which the BSU is operating. For 400/275 kV and 132 kV systems, the range remains 35–50 MW; for 33 kV systems, the recommended range is 10–20 MW; and for 11 kV systems, it is 0.4–1 MW.

2.2.3. Frequency and Voltage Control

This relates to maintaining frequency and voltage within acceptable limits during block loading. The frequency must remain within the range of 47.5 Hz to 52 Hz or 49 Hz to 52 Hz as specified by Elia.

In terms of voltage control, NGESO stipulates that the voltage should remain within ±10% of its nominal value, whereas Elia defines voltage limits based on the block loading conditions and the energisation time frame [20].

For restoration involving offshore wind power plants, the control of frequency and voltage should be managed by the wind farm itself and, where necessary, supported by an external power supply with frequency support and/or reactive power capability.

2.2.4. Reactive Capability

The NGESO mandates that wind farms possess a reactive power capability of 50 MVar, while conventional generators are required to provide 100 MVar. Conversely, Elia sets different reactive power requirements for various BS zones, with standards in Belgium typically ranging from 30 to 50 MVar at the low-voltage side of the step-up transformer. Shunt reactors can assist in meeting these reactive power needs [20,21]. Long cables operating under low-load conditions can generate substantial amounts of capacitive reactive power, which the BS unit must absorb. Reactive capability involves not only the ability to energise the transmission network without active power (reactive power at zero crossing) but also the management of magnetic inrush and transient voltages during energisation.

2.3. Scenarios to Energise OWPPs

In this section, different scenarios for energising an OWPP are discussed. A BSU needs to self-energise and contribute to network reconfiguration. Traditionally, such units use a small cranking generator, such as a DG, for this purpose. For OWPPs, an APS like a synchronous DG or a BESS can be used to start wind turbines. Alternatively, GFM WTs can self-start. The size of the cranking unit needs to have enough energy to start key components that enable power generation. These include the wind turbine controllers and communications, heating and cooling loads, water and oil pumps, and motors such as the pitch and yaw. According to [23], the auxiliary power needed to self-start a wind turbine is less than 5% of its rated power.

The SIF Blade project explored four energisation solutions, with two selected for further study. These solutions vary based on the APS location and the requirement for GFM WTs. An APS, if located onshore or offshore, can provide a stable voltage reference, eliminating the need for GFM WTs as all GFL WTs will synchronize with the APS voltage. Self-starting wind turbines must be GFM-capable. The four scenarios considered in this study to energise the OWPP may be seen in Table 1.

Table 1. Scenarios for WT-OWPP Energisation.

Scenario	APS Location	GFM WT Required?
S1	Onshore	No
S2	Self-start WT	Yes
S3	Offshore	No
S4	Hybrid	No

Figure 1 graphically illustrates the locations of S1, S2, and S3; S4 is a combination of these APSs. In the figure, S1 is situated in the onshore substation, along with several loads, the local network, and a variable shunt compensation. S2 represents an APS located inside a WT, indicating a self-starting WT. S3 is positioned in the offshore substation, following the offshore transformer and static shunt reactive compensation but before the HVAC export submarine cable.
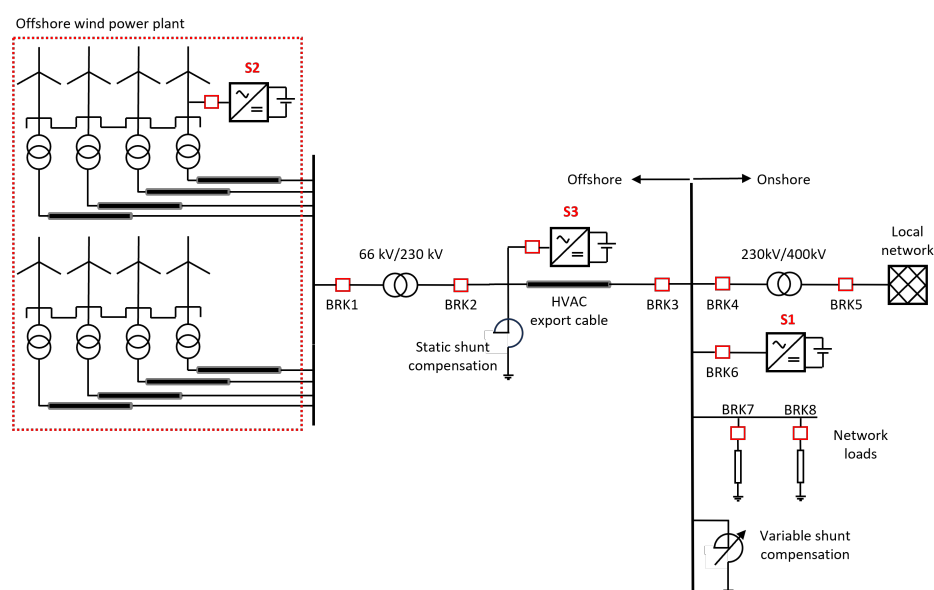

Figure 1. One-line diagram of studied system with the different APSs located onshore, offshore, and inside WTs (self-start scenario).

Scenario 1 (S1) involves placing the APS at an onshore substation. The APS would need to energise all equipment from the substation to the OWPP, including the substation itself, reactive power shunt compensations, offshore submarine HVAC export cable, OWPP array cables, and finally the wind turbines. Although this process requires significant energy, the onshore location of the APS allows for larger units due to space availability, unlike offshore substations or wind turbines. Additionally, APS units are typically already available at or near onshore substations. Scenario 1 is thus an attractive solution due to its simplicity and technology readiness. Located onshore, the APS is easier to install, operate, and maintain, with no space limitations. It can keep a stable voltage reference signal, eliminating the need for GFM wind turbines.

Scenario 2 (S2) considers self-starting wind turbines which have the capability to energise themselves. This is accomplished via an uninterruptible power supply (UPS), a small BESS, or a diesel generator inside a wind turbine. Such wind turbines would need to be equipped with grid-forming converter control technology as to be able to keep a constant and reliable voltage source reference signal. Once one or several self-start GFM wind turbines are energised, these units are responsible for providing enough energy to energise the OWPP array cables and the GFL wind turbines, which would then synchronise with the GFM units.

Previous studies have explored the concept of self-start wind turbines for OWPPs. In [24], a method is proposed where wind turbines start using their internal energy storage without external generators. In [25], an autonomous startup and synchronization using the wind turbine APS to sequentially energise turbines is discussed. Additionally, in [26], a wind turbine equipped with a DG that can generate power during a blackout is introduced, replicating the electricity network and supporting auxiliary devices.

In Scenario 3 (S3), an APS is located in the offshore substation. Firstly the offshore transformer and substation equipment are energised and then the OWPP itself, reducing energisation time compared to an onshore APS. The offshore industry, particularly the oil and gas sector, is familiar with APSs in offshore substations, and battery energy storage systems (BESSs) are a topic of interest for such platforms [27–31]. However, limited space in offshore substations makes it challenging to include a BESS unit solely for black-start purposes if the OWPP is already constructed. Scenario 3 is the most expensive due to higher installation and maintenance costs and limited accessibility. Although grid-forming wind turbines are recommended, they are not necessary as the APS can generate frequency and voltage. Some offshore substations may already have an APS capable of cranking the first wind turbine, providing an alternative for auxiliary power.

Scenario 4 (S4) proposes a hybrid solution combining onshore and offshore auxiliary power supplies. For example, an onshore BESS could work alongside GFM self-start wind turbines or an additional offshore BESS. This approach reduces costs and improves accessibility compared to other scenarios while also increasing available energy and redundancy. Some studies already mention this alternative [32–34]. This hybrid configuration leverages the advantages of both onshore and offshore setups, ensuring a more flexible energisation process for the OWPP.

For this project, Scenarios 1 and 2 were selected based on their advantages. Scenario 1 was chosen primarily due to the existing readiness of technology and the availability of onshore APS units for future tests. An onshore APS not only facilitates the energisation of the OWPP but also provides additional benefits such as voltage and frequency regulation if necessary. Further, since this unit is bigger, it might be able to sustain a voltage reference signal for longer. Scenario 2 was selected due to the project's high level of expertise and the interest from various partners in utilizing self-starting, GFM wind turbines. This scenario is cost-effective and offers a shorter restoration time, making it a practical choice for efficient and rapid energisation. In this paper, for both EMT and SSM analysis, only Scenario 2 was considered.

3. System Under Study

In this section, the hardware and the converter control strategies used throughout this study are introduced. While the hardware configuration varies depending on the specific scenarios discussed, these changes are detailed in their respective sections. This section provides a baseline description of the hardware analysed. All system components, including the hardware and control strategies, and all the analyses performed, were modelled and simulated using MATLAB/Simulink R2023a, software widely recognised for its robust capabilities in power system analysis. MATLAB/Simulink was chosen to ensure accurate representation of the system dynamics and control interactions, forming the foundation of the simulations conducted in this study.

3.1. System Modelling

Figure 1, introduced previously, shows a one-line diagram of the model used throughout this paper, although some changes will be made to this model in each section. The diagram illustrates a system comprising an OWPP with a BESS and a self-starting, grid-

forming wind turbine. In the figure, the OWPP connects to the power system via an offshore transformer, which steps up the voltage from 66 kV to 230 kV. This voltage is transmitted through a submarine export HVAC cable with a length of 50 km. The cable benefits from two shunt reactor compensations: a static one located offshore at the beginning of the cable (included in the offshore substation for practical purposes) and a variable one in the onshore substation. These compensations address the high capacitance of the submarine cables.

The system also includes an onshore transformer, which steps up the voltage from 230 kV to 400 kV and a local network operating at 400 kV. This local network, displayed after BRK5, represents the target area for power system restoration and contains critical loads modelled as impedances. These critical loads serve as proxies for essential consumers, including hospitals, emergency services, and other high-priority infrastructures. The grid specifications include a short-circuit ratio of 1.5. These components are crucial for assessing the ability of the system to restore power under varying conditions.

The OWPP can operate either as a top-up or an anchor BSU generator during the power system restoration process. In the top-up scenario, the OWPP contributes active and reactive power to an energised grid. In the anchor scenario, it actively participates in network reconfiguration and block loading. The staged process aligns with the classical PSR framework of black start, network reconfiguration, and load restoration, as described earlier in Section 2. Self-starting GFM wind turbines initiate the black start process by establishing an energised path. Subsequently, the rest of the GFL and/or GFM units are energised to build the skeleton network and supply critical loads.

The designed hardware system employs full back-to-back converters for each wind turbine in the OWPP. However, for this study, the configuration is simplified using an aggregated wind farm model to focus on the system-level dynamics. This aggregated model captures the essential characteristics of the OWPP while reducing computational complexity.

Furthermore, the breakers shown in the figure are included to test the energisation process, study possible transients (especially during transformer energisation and the energisation of cables and shunt reactors), and verify whether the EMT simulations meet the TSO technical requirements specified earlier.

As the hardware system will vary depending on the study presented, the parameters utilised are described in each section.

3.2. Converter Control Strategies

Two converter control units were used in this study, a GFM one and GFL one. This section describes both, which may be seen in Figure 2. Further, the parameters of the controllers used in this study may be seen in Appendix A and Tables A4 and A5 for both grid-forming and grid-following controllers, respectively. Further, a supervisory frequency controller was designed and is also explained in this section.

3.2.1. Grid-Forming Unit

The GFM unit used in this study is called the virtual synchronous machine (VSM) and is based on the studies described in [35–38]. The name was given as it emulates through its controllers the behaviour of a synchronous machine. A diagram of the VSM may be seen on the right side of Figure 2. It consists of two PI controllers: one is referred to as the power loop (P/f loop) and the other the voltage loop (Q/V loop). Further, a virtual impedance was added to this controller due to the transients that may happen throughout the energisation process of the power system.
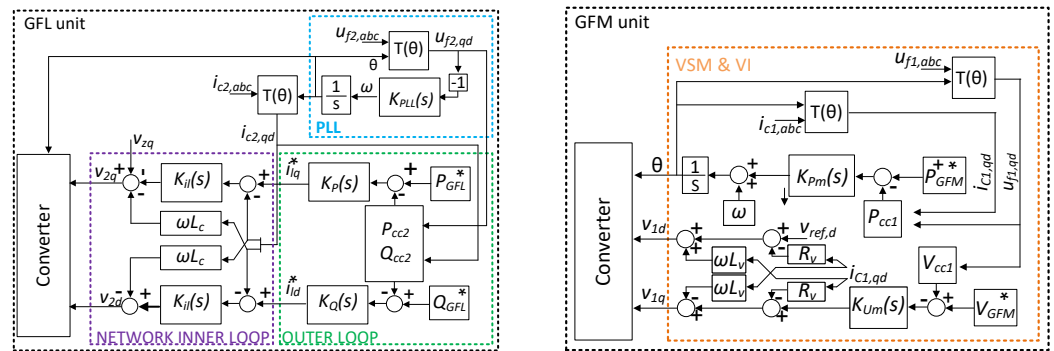
Figure 2. GFL and GFM control structure schemes.

The power PI controller computes the angle of the point of common coupling (PCC). The voltage PI controller computes the v_q component of the voltage to be fed to the converter and the v_d component is zero. Thus, the Clark transformation is used instead of the Park transformation.

From the figure, the power PI controller $K_{Pm}(s)$ is defined as shown in Equation (1).

$$K_{Pm} = m_p + \frac{m_i}{s} \tag{1}$$

where m_p is the proportional gain and m_i the integral gain of the power controller. With regards to the voltage controller, the PI is defined as follows:

$$K_{Um} = k_{p,VCC} + \frac{k_{i,VCC}}{s} \tag{2}$$

where $k_{p,VCC}$ is the proportional term and $k_{i,VCC}$ the integral term.

Several studies were analysed with regards to virtual impedance implementation [39–43], and eventually the approach described by Rodriguez-Cabero et al. described in [43] was followed. The virtual impedance is located after the PI voltage controller. Thus, the q component of the voltage that is fed back to the converter, v_{lq}, is given by

$$v_{lq} = (V_Z^* - u_{f1,q})\left(k_{p,VCC} + \frac{k_{i,VCC}}{s}\right) - i_{c1,q}R_v - i_{c1,d}L_v\omega \tag{3}$$

where V_Z^* is the voltage reference of the controller, $u_{f1,q}$ is the q component of the voltage at the PCC of the grid-forming converter, and $i_{c1,q}$ and $i_{c1,d}$ are the synchronous reference frame components of the current measured at the converter terminals. For the d component of the voltage at the converter terminals, v_{ld} is given by

$$v_{ld} = -i_{c1,d}R_v + i_{c1,q}L_v\omega \tag{4}$$

In both Equations (3) and (4), R_v and L_v are the virtual resistance and inductance and ω is the frequency measured at the PCC.

3.2.2. Grid-Following Unit

The grid-following controller here used is called the Standard Vector Current Controller (SVCC) and it was based on the one that may be found in [44]. Its scheme may be seen in the left side of Figure 2. It consists of a PLL, a current inner loop, and voltage and power outer loops. The PLL has the objective of computing the angular velocity of the electrical network. To do so, a PI controller is implemented as displayed in Equation (5).

$$K_{PLL} = k_{p,PLL} + \frac{k_{i,PLL}}{s} \tag{5}$$

where $k_{i,PLL}$ is the integral gain and the proportional term is $k_{p,PLL}$. The inner loop is the lower-level control of this GFL unit. It allows the independent control of both q and d components due to its decoupling terms. The output of this controller is the voltage which is fed back to the converter. The control of both components in the synchronous frame is performed via PI controller as shown in Equation (6).

$$K_{il} = k_{p,il} + \frac{k_{i,il}}{s} \tag{6}$$

where $k_{i,il}$ is the integral gain and the proportional term is $k_{p,il}$. The outer loop controller computes the current references in the synchronous frame i^*_{cq} and i^*_{cd} which are later fed into the inner loop controller. This is performed considering the active power and voltage magnitude of the system. Both voltage and power outer loops are also controlled with PI controllers as shown in expressions (7) and (8), respectively.

$$K_P = k_{p,PC} + \frac{k_{i,PC}}{s} \tag{7}$$

$$K_V = k_{p,VC} + \frac{k_{i,VC}}{s} \tag{8}$$

where $k_{p,PC}$ and $k_{p,VC}$ are the proportional gains of both power and voltage outer loop controllers and $k_{i,PC}$ and $k_{i,VC}$ are the integral gains.

3.2.3. Supervisory Frequency Support Controller

Standard GFL wind turbines often face frequency stability problems and typically lack droop control [45]. When restoring the power system, various voltage and frequency disturbances can occur, which the standard GFL controller, shown in Figure 2, does not address. To manage these issues without altering the existing controller structures, an external supervisory controller was developed to help prevent frequency drops during load restoration.

This external controller provides frequency support, similar to how a governor functions in a synchronous generator. It uses a PI controller integrated with both GFM and GFL loops. The controller adjusts the active power references in both GFM and GFL systems to keep the frequency within acceptable limits set by the TSO. The power adjustment is shared between the GFM and GFL controllers based on the level of GFM penetration, as shown in Figure 3. The controller reacts to frequency deviations ($f^* - f_{PCC}$) by distributing a power increment ($x\%$ and $1 - x\%$ of ΔP) between the GFM and GFL controllers.
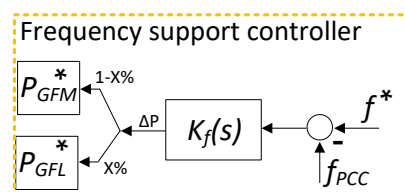

Figure 3. Diagram of the supervisory frequency support controller.

4. Steady State (P,Q) Operating Points

The aim of this study was to assess if the offshore wind power plant connected to the power system introduced before could generate, in steady state, an envelope of active and reactive power (P,Q) operating points that would encapsulate the local network (P,Q) needs, thereby matching local network demand. The network demand was provided in terms of (P,Q) operating points, for different wind speeds, demands, and paths in the UK.

To examine the steady-state operating conditions, a power flow analysis was conducted. Firstly, the hardware model described in Section 3 was simplified to achieve an impedance model, facilitating the utilization of a Thevenin equivalent for the purpose.

Subsequently, the local network demand data were assessed. Once this step was completed, the voltage magnitude and angle of the OWPP were varied to delineate its operational envelope and understand if it effectively encapsulated the operation points of the local network. This iterative process was carried for various conditions, changing the wind speed and local network demand.

4.1. Impedance Model and Thevenin Equivalent

The hardware model shown in Figure 1 was simplified using passive components for this study, as may be seen in Figure 4. This simplification was performed to enable a power flow analysis via Thevenin equivalent impedance. In this figure, an aggregated offshore wind farm is represented with a voltage source E and its LC filter via R_c and L_c. The offshore transformer is represented by R_{ot} and L_{ot}. The model also includes offshore shunt compensation with L_l and R_l and onshore shunt compensation with L_r and R_r. The export cable is modelled as a π cable with parameters C_{hv}, R_{hv}, and L_{hv}. Additionally, the grid line is represented with parameters R_g and L_g and is connected to a load, Z_{LD}.
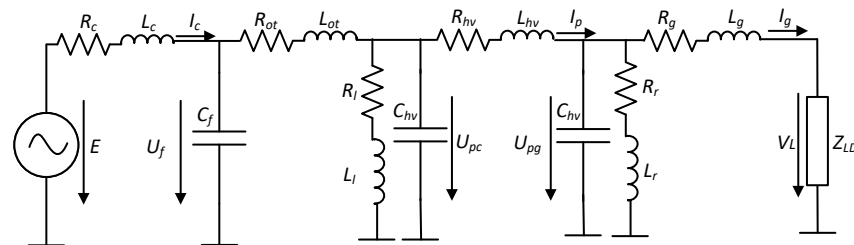

Figure 4. OWPP and network simplified one-line model.

The system represented in Figure 4 was further simplified in impedances as may be seen in Figure 5. This way, the entire system was encapsulated only considering a voltage source with varying magnitude, $\overline{E}$, and angle, α, an equivalent impedance representing all the system components, and the load. This way it was possible to vary the impedance depending on the system parameters such as OWPP nominal power output, local network demand, and wind speed and analyse the impacts on the load, which here represents the local network demand, as will be explained in the next section.
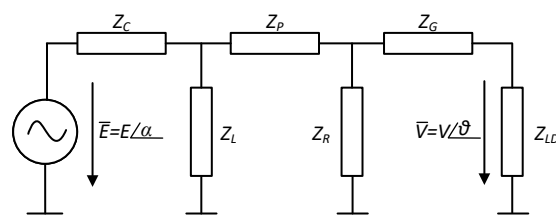

Figure 5. OWPP and network one-line impedance base model.

From Figure 5, the final Thevenin voltage and impedance are given by

$$V_{th} = \overline{E} \cdot \frac{Z_C \cdot (Z_L + Z_P + Z_R)}{Z_L \cdot (Z_P + Z_R) + 2Z_C \cdot (Z_L + Z_P + Z_R)} \tag{9}$$

$$Z_{th} = \frac{Z_C Z_L Z_R + Z_P Z_R}{Z_C Z_L + Z_P(Z_C + Z_L) + Z_R} + Z_g \tag{10}$$

where V_{th} is the Thévenin voltage and Z_{th} the Thévenin impedance. This impedance will be later used having its real part, R, and imaginary one, X, separated.

Considering the Thévenin equivalent described by Equations (9) and (10), the current flowing through the converter is

$$\overline{I} = \frac{\overline{E} - \overline{V_{th}}}{Z_{th}} \tag{11}$$

The apparent power, S, at the converter terminals is

$$S_c = \overline{V_{th}}\,\overline{I}^* = \overline{V_{th}}\left(\frac{\overline{E_s} - \overline{V_{th}}}{Z_{th}}\right)^* \tag{12}$$

Developing this equation and separating the real and imaginary parts, the active and reactive power flow equations for the power converter are achieved.

$$P_c = \frac{R\overline{V}\overline{E}cos(\alpha) - \overline{E}\overline{V}Xsin(\alpha) - \overline{V}^2R}{R^2 + X^2} \tag{13}$$

$$Q_c = \frac{X\overline{V}\overline{E}cos(\alpha) - \overline{E}\overline{V}Rsin(\alpha) - \overline{V}^2X}{R^2 + X^2} \tag{14}$$

4.2. Local Network Loads

As stated in the grid codes of the UK regarding power system restoration, dispatched providers all together need to be able to restore 60% of the network demand in the first 24 h and 100% in 72 h. This energisation is performed in steps of active and reactive power. Depending on several conditions such as the number of generators available, demand, and wind speed conditions, black start generators will be chosen to be part of the energisation process, be that of network reconfiguration or block loading.

The data here considered to study the capabilities of an OWPP to meet local network demand are based on real data provided by a party of the SIF Blade project. It is assumed that a local substation demands active and reactive power in steps to energise several loads. This energisation process is depicted in Figure 6 for three different cases where demand, energisation path, and wind speed vary. These are the three load demand cases that shall be studied in the this section.
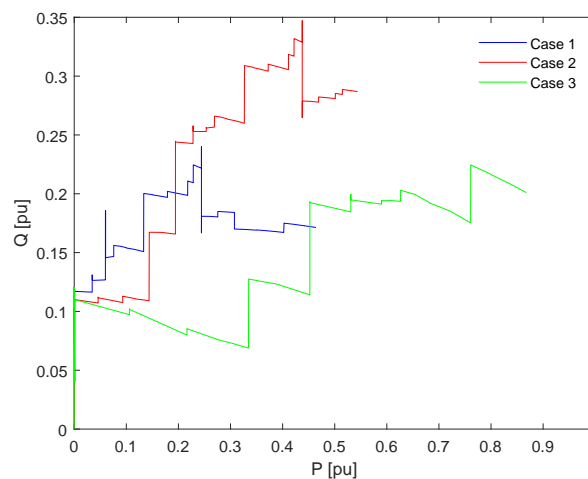

Figure 6. Energisation steps for three different local network demand cases, 1, 2, and 3.

4.3. Case Studies

In a controlled OWPP, the voltage magnitude and angle output are regulated by the action of the converter controller. However, in this case where the interest was to compute operating points via power flow, the model shown in Section 4.1 was utilised and the operating points of the system computed using the previous Equations (13) and (14).

For each case introduced previously in Section 4.2, the output voltage and angle at the terminals of the converter were varied to create the operating region of the OWPP. The voltage magnitude and angle were varied to create the operating region of the OWPP while ensuring compliance with NGESO requirements. Specifically, the voltage variations were constrained to within ±10% of the nominal value, in line with NGESO specifications. The angle variations were adjusted to reflect realistic operating conditions from SIF BLADE partners, ensuring that the resulting operating region accurately captured the performance of the system under typical and extreme scenarios.

The wind speed used in this analysis was given by an SIF BLADE project party. This quantity was varied between 0 and 1, where 1 would mean rated wind speed and 0 no active power production. Hence, to compute the active and reactive power available, the apparent power was multiplied by the wind speed ratio.

Table 2 displays the wind speed used for each case, the converter terminal angle, and voltage magnitude that were needed to generate the OWPP envelope. Figure 7 displays the results of the envelope for the three study cases. Results have shown that the OWPP connected to the power system considered was able to create an area of operation capable of enveloping the local network demand for three different study cases where the wind speed and demand changed the active and reactive power operating points in the local network.

This was achieved without varying any parameter in the impedance model, as introduced in Equations (9) and (10). Thus, there is margin to vary even further the converter terminal voltage magnitude and angle to accommodate local network demand, as well as potentially increase or decrease the shunt compensation that exists in the model. Further, the study here presented was performed for a cable length of 50 km, and hence the impact of the capacitance of the HVAC cable did not play a major role in active power losses nor reactive power needs. If such an issue arises, as it was was previously observed in [46], these components significantly impact the voltage stability of the system in steady state, as well as the (P,Q) operation envelope which the OWPP may provide to the local network, and this study may be carried out varying the shunt impedance to analyse how much reactive power would need to be compensated.

Table 2. Wind speed, converter voltage angle, and magnitude for the different study cases.

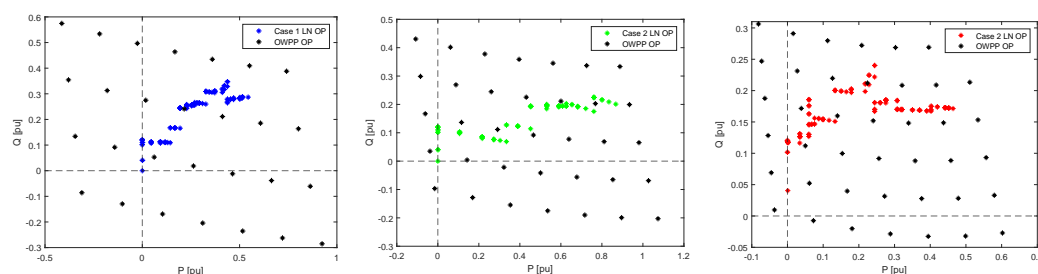| Case	Wind (%)	$\angle \delta^\circ$	$\overline{E_s}$ (pu)
1	0.15	-5 to 2	0.95 to 1.02
2	0.6	-10 to 3	0.91 to 1.01
3	0.35	-8 to 2	0.93 to 1.02

Figure 7. OWPP and local network (P,Q) OP for cases 1, 2, and 3.

5. Grid-Forming Penetration—EMT Studies

This section presents the EMT studies conducted to analyse the time domain performance in the PSR process. The aim was to determine if different levels of grid-forming

penetration would meet some of the technical requirements set by the TSO. The requirements examined are described in Table 3. In this study, the GFM penetration was varied between 0% and 100% in steps of 20%.

Table 3. Technical requirements analysed via EMT simulations.

No.	Technical Requirement	Range
1	Block loading capability	35 to 50 MW
2	Frequency control (while block loading)	47.5 to 52 Hz
3	Voltage control (while block loading)	0.9 to 1.1 pu ($\pm$10%)
4	Ability to withstand inrush currents and transient voltages	Analysed during network energisation
5	Reactive range to energise immediate network	50 MVAr

Figure 8 displays a one-line diagram of the model used for the time domain studies and Appendix A contains the parameters that were used in this study. To analyse the optimal grid-forming penetration, the aggregated wind farm was split into two parts, each with a controlled voltage source converter (with voltages V_1 and V_2) and their LC filters (parameters R_c and L_c), representing both GFM and GFL converter penetrations. This setup allowed for varying the percentage of GFM penetration.

The model further includes an offshore transformer that steps up the voltage from 66 kV to 230 kV. An HVAC export cable is represented using a π equivalent model with parameters R_{hc}, L_{hc}, and C_{hc}. This cable has a length of 50 km. Due to the high capacitance of submarine cables, two shunt reactive power compensations were included: one fixed offshore (L_l and R_l) and one variable onshore (L_r and R_r). Four RC loads were connected to simulate the block loading capabilities. The active and reactive power steps and respective values of R_{LD} and C_{LD} may be seen in Table A2 of Appendix A.
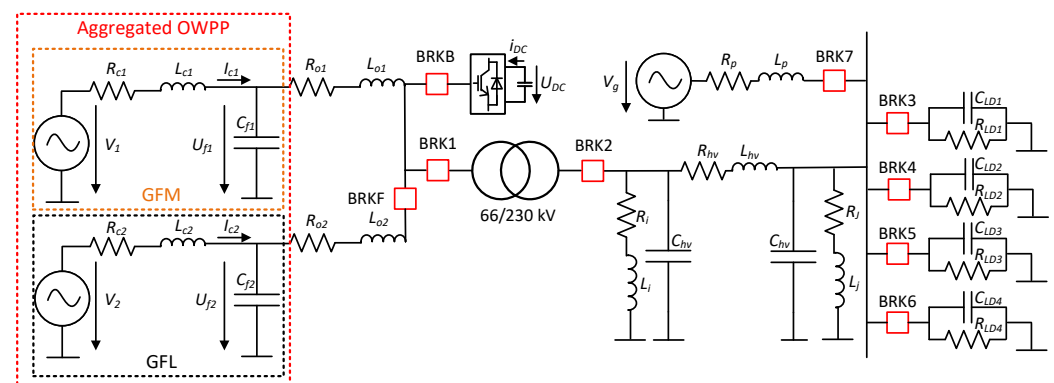

Figure 8. One-line diagram of the EMT model analysed with the aggregated OWPP encapsulating both GFM and GFL wind turbines.

Additionally, the scenario tested here is Scenario 2, involving self-starting wind turbines, with a BESS connected via breaker BRKB to the upper branch of the OWPP. Although the BESS may have several purposes, in this study, it was only used for wind farm energisation. It should also be noted that an aggregated wind farm model was used in this study, so array cables of the wind farm and wind turbine transformers were not considered, but their study is considered as future work. Furthermore, only the offshore transmission system was considered as no onshore cables were modelled for this study. Furthermore, both top-up and anchor generation scenarios were used. In case of the top-up scenario, as an external grid is present during the energisation process, breaker BRK7 is closed. In the case of anchor generation, BRK7 was open through all the simulations, and hence no external grid support was available.

5.1. Energisation Sequence

The energisation process is detailed in Table 4. It begins by energising one or several self-start-capable WTs (depending on the percentage of GFM penetration) by closing breaker BRKB. In this study, all GFM WTs are assumed to be self-start-capable. Once these units are energised, breaker BRKF is closed to energise the rest of the OWPP, including the GFL units. This step introduces synchronisation challenges due to the connection of multiple wind turbines, each requiring precise coordination to ensure stable operation. Since this study involves an aggregated wind farm model, the resulting transients may not accurately represent the actual events and this topic is not discussed here; however, it will be addressed in future research.

After the OWPP is fully energised and operating in islanded mode, breaker BRK1 is closed to energise the offshore transformer. This step presents technical challenges which are addressed in technical requirement number 4, displayed in Table 3. To address this issue, the point-on-wave (POW) strategy was employed. Several studies discuss the mitigation of inrush currents [47–50], so this topic will not be fully explored here. However, a brief description of the POW strategy is provided below due to its application in this study.

After energising the offshore transformer, breaker BRK2 is closed to energise the shunt compensations and the HVAC export cable. It should be noted that in a real-world scenario, these components would likely be energised separately. This step also presents challenges related to transient performance during energisation or de-energisation processes. These transient phenomena can result in inrush currents, high overvoltages, current zero-miss, and transient recovery overvoltages in circuit breakers. These phenomena will depend on the length of the cable, power-frequency voltage, system short-circuit power, shunt compensation, and switching instant and may be mitigated applying proper shunt compensation, closing a circuit breaker at a specific time or using a pre-insertion resistor [50–54].

Once the path from the OWPP to the onshore network is fully energised, the process of block loading starts. Subsequently, BRK3 is closed, followed by BRK4, BRK5, and BRK6 to energise the RC loads representing the active and reactive power demand from the local network. These loads were energised every two seconds.

Table 4. Energisation sequence of PSR.

Step	Time (s)	Activity
1	0	BRKB is closed and self-start GFM units start the energisation process
2	2	BRKF is closed to energise the GFL units, hence fully energising OWPP
3	3.2	BRK1 is closed and offshore transformer is energised
4	5	BRK2 is closed, energising shunt compensations and submarine export cable
5	7	BRK3 is closed to energise first load (P1)
6	9	BRK4 is closed and second load is energised (P2)
7	11	BRK5 is closed and third load is energised (P3)
8	13	BRK6 is closed and fourth load is energised (P4)

5.2. Results

This section displays the results of the EMT simulations. For each step of energisation, it was seen whether the TSO requirements mentioned in Table 3 were met. The section is split as follows: Section 5.2.1 introduces the transformer energisation; Section 5.2.2 introduces the shunt reactors and cable energisation; and Section 5.2.3 displays the results of the block loading for both top-up and anchor scenarios. In Section 5.3, final results are displayed and conclusions drawn.

5.2.1. Transformer Energisation

The energisation of a transformer may result in inrush currents due to the saturation of its core. Several strategies were studied in academia such as the pre-insertion resistor, point on wave (controlled switching), and sof-start. These may require changes in the converter control strategy or even in the transformer hardware. These strategies are detailed in the following studies [48,50,55–59].

Due to its simplicity, the classic controlled switching strategy (POW) was used in this study. This technique relies on closing the breaker of the offshore transformer at an instant at which the residual flux is equal to the prospective flux, that is, at an optimal closing angle α. This may be seen through Equation (15), where the instantaneous flux is calculated [57].

$$\phi \approx \frac{-L_m V_P cos(\omega t + \alpha)}{\sqrt{R_1^2 + (\omega L_T)^2}} + \left(\phi_r + \frac{L_m V_P cos(\alpha)}{\sqrt{R_1^2 + (\omega L_T)^2}} \right) e^{-\frac{R_1}{L_T} t} \tag{15}$$

where ϕ is the core flux, V_P is the voltage of the energised transformer primary, L_m is the core inductance, L_T is the primary inductance summed with the core inductance, R_1 is the primary resistance, ω is the angular frequency, and α is the angle at which the breaker is closed and the transformer energised. If the residual flux is equal to the prospective flux, the decaying term in Equation (15) is eliminated and thus the inrush currents neutralized.

The prospective flux can be estimated using Equation (16). This equation shows that the prospective flux is obtained by integrating the voltage applied to the energised (primary) side.

$$\phi_p = \int V_P sin(\omega t) dt \tag{16}$$

For this study, the parameters of the transformer used may be seen in Table A3. Firstly, a simulation was analyzed without any inrush current mitigation strategy; thus, the breaker was closed at a random instant of t = 3.3 s. Results of this simulation may be seen in Figure 9. From this figure, it is noted that the transformer suffers severe inrush currents on the order of 10 kA and voltages at both primary and secondary go above and below TSO allowed limits.
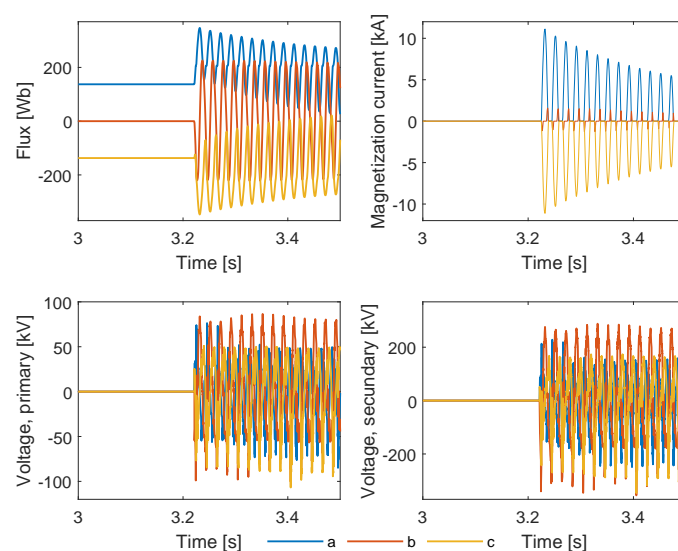

Figure 9. Offshore transformer energisation without any inrush current mitigation technique.

Figure 10 displays the results of the offshore transformer energisation using the POW energisation strategy for a GFM penetration of 20%. For the residual flux considered

(which may be seen in Table A3) of 0.8 pu, the optimum instant of closing the breaker was computed at t = 3.2117 s. In this figure, it may be seen that the inrush currents are mitigated, with the maximum inrush current being 5 A. Both primary and secondary voltages of the transformer are within acceptable TSO limits.
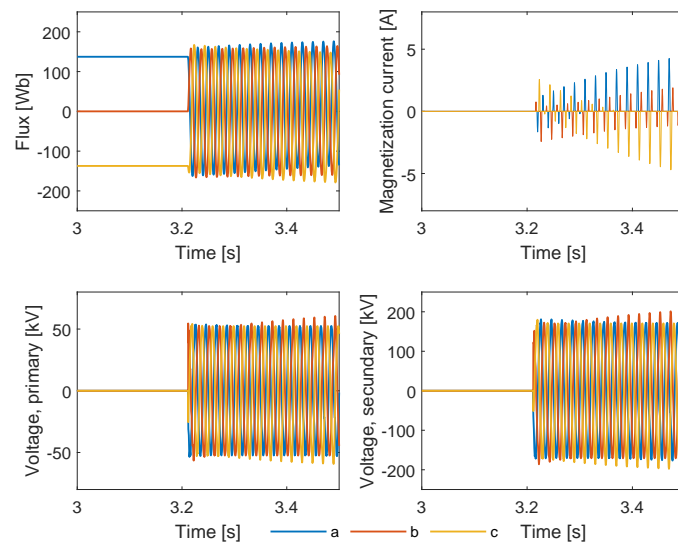

Figure 10. Offshore transformer energisation with POW for a GFM penetration of 20%.

The POW strategy was applied for various percentages of GFM penetration. This strategy effectively mitigated inrush currents in all cases, as may be seen in Figure 11.
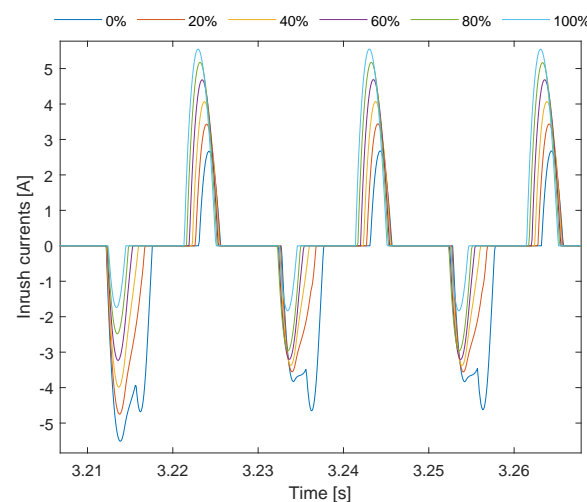

Figure 11. Inrush currents after transformer energisation for different GFM penetration percentages.

However, the magnitude of the inrush currents varied slightly depending on the GFM penetration. This variation occurs because, at the computed instant when the breaker is closed, the voltage on the primary side of the transformer differs slightly, leading to slight variations in the prospective flux. Since the optimal breaker closing angle is based solely on the residual flux within the transformer core, the prospective flux and residual flux will not be exactly identical, resulting in slight differences in inrush current magnitudes. Additionally, it was seen that the offshore transformer is energised only after the GFL units are synchronized with the GFM units and the OWPP is running in islanded mode, which can cause some voltage distortions. Allowing time for the waveform to stabilize and return to its natural sinusoidal form before energising the transformer is necessary; otherwise, undesired inrush currents may occur. Despite these variations, the POW strategy

successfully mitigated inrush currents across all levels of GFM penetration, demonstrating its effectiveness regardless of penetration levels.

5.2.2. Shunt Reactors and Export Cable Energisation

After energising the offshore transformer, breaker BRK2 was closed to energise the offshore HVAC submarine cable, along with both offshore and onshore shunt compensations. The offshore reactor is static, while the onshore compensation is variable. This means that the onshore compensation value will adjust based on the reactive power requirements, which might differ for normal operation, energisation, or de-energisation.

As previously mentioned, the submarine cable is 50 km long and produces significant capacitive reactive power. A load flow analysis was conducted to design the shunt compensations to mitigate this reactive power, ensuring that the cable voltage remains within acceptable TSO limits and the power factor stays close to unity at the PCC. It was concluded that 270 MVAr would be compensated via shunt reactors, and 40% of this quantity would come from the offshore reactor and 60% from the onshore one.

To prevent overvoltages and the zero-missing phenomenon, which occur when reactive power compensation exceeds 60% due to interactions between inductive and capacitive components in both the cable and reactors, a Pre-Insertion Resistor (PIR) was implemented. Additionally, incorporating two shunt compensations, rather than just one onshore, was a critical measure to mitigate these phenomena.

The value of the PIR and the optimal switching time for its connection depend on several factors, including the shunt compensation level and the length of the export submarine cable. The PIR also plays a crucial role in mitigating inrush currents that arise from interactions between the offshore transformer, the export cable, and the shunt components.

For this study, the PIR was designed with a resistance of 30 Ω, and the breaker was closed 100 ms after BRK 2. The results are presented in Figure 12. This figure shows that the zero-missing phenomenon was eliminated, and no significant overvoltages occurred. Additionally, inrush currents were effectively mitigated.
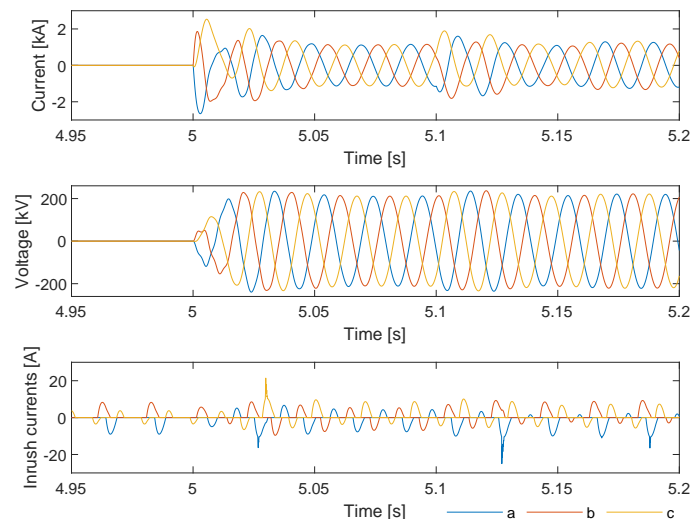

Figure 12. Cable and shunt reactor compensation for a GFM penetration of 40%.

Figure 13 displays the inrush current results for different GFM penetrations. It can be observed that while inrush currents vary slightly depending on the level of GFM penetration, the differences are minimal. Thus, it can be concluded that across all GFM penetrations, the cable and shunt compensations were energised with minimal impact.
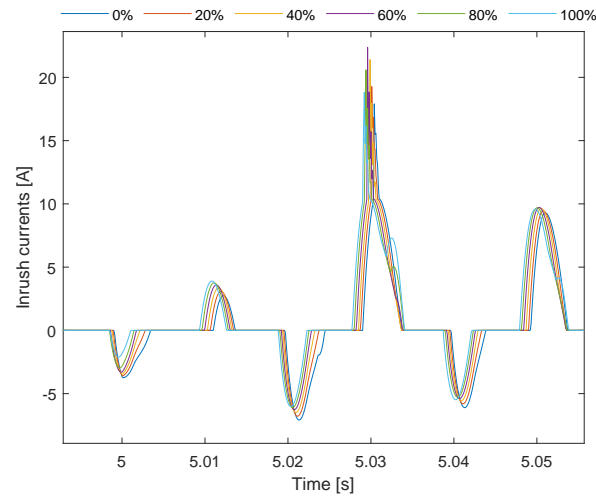
Figure 13. Inrush currents after cable and shunt compensation energisation for different GFM penetration percentages.

5.2.3. Block Loading

Block loading capabilities were analysed for both anchor and top-up generation scenarios. For both cases, reactive capability was also analysed as shown in Table A2. The results depicted in Figure 14 illustrate the block loading results for the top-up scenario for an 80% GFM penetration. It can be seen that the active power at the load is well achieved and both GFM and GFL controllers follow its reference as expected.
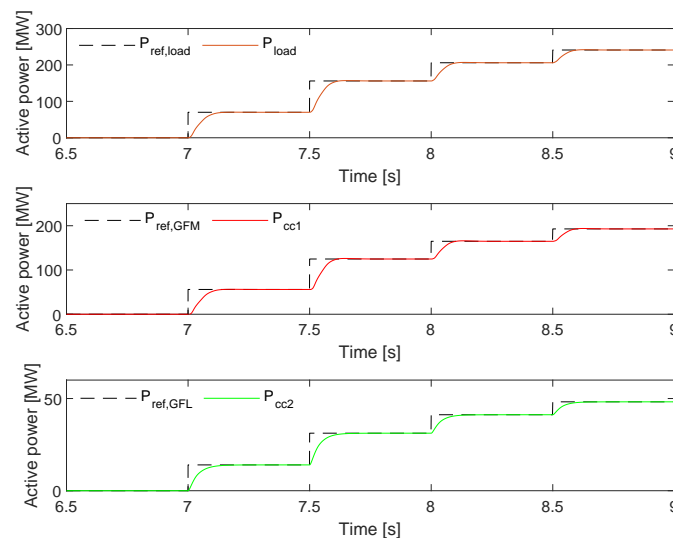

Figure 14. Active power at the load and converter control action (GFM and GFL) for an 80% GFM penetration during block loading for the top-up scenario.

Figure 15 depicts the voltage and frequency responses for the top-up generation scenario under varying levels of GFM penetration, ranging from 0% to 100%. Across all scenarios, the voltage remains well within the TSO acceptable limits of 0.9 to 1.1 pu. This indicates that the integration of OWPP, irrespective of the penetration level of GFM capability, does not adversely affect voltage stability. The system maintains a robust voltage profile, showcasing the efficacy of the external grid stabilizing influence.

The frequency response similarly remains within the TSO acceptable range of 47.5 to 52 Hz, demonstrating overall stability. However, the data reveal that as the percentage of GFM penetration increases, there are higher frequency peaks. Despite these peaks, the frequency deviations are minimal and transient, quickly returning to the nominal

value of 50 Hz. This suggests that while GFMs contribute positively to grid stability, their increased penetration introduces minor fluctuations in frequency. This could be due to the more active role these OWPPs play in frequency regulation, providing quicker but slightly more variable responses to changes in load. The presence of the external grid buffers the system against significant frequency and voltage variations, enabling the OWPP to function effectively within the required operational parameters.
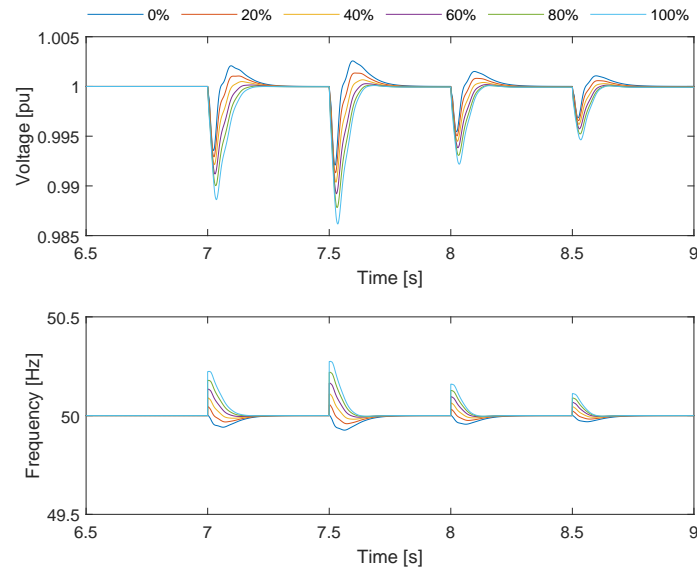

Figure 15. Voltage and frequency at the PCC during block loading for the different GFM penetrations (from 0% to 100%) for the top-up scenario.

Regarding the anchor scenario, the block loading results were similar in that the load received the necessary power. However, the frequency and voltage responses were distinct because no external grid supported the system energisation. The top figure in Figure 16 illustrates the frequency and voltage results. While the voltage remains within acceptable TSO limits, the frequency drops significantly, with the worst case occurring at 0% GFM penetration, with the frequency dropping to 42 Hz. Higher GFM penetration results in a smaller frequency drop due to the droop characteristics of the GFM controller.
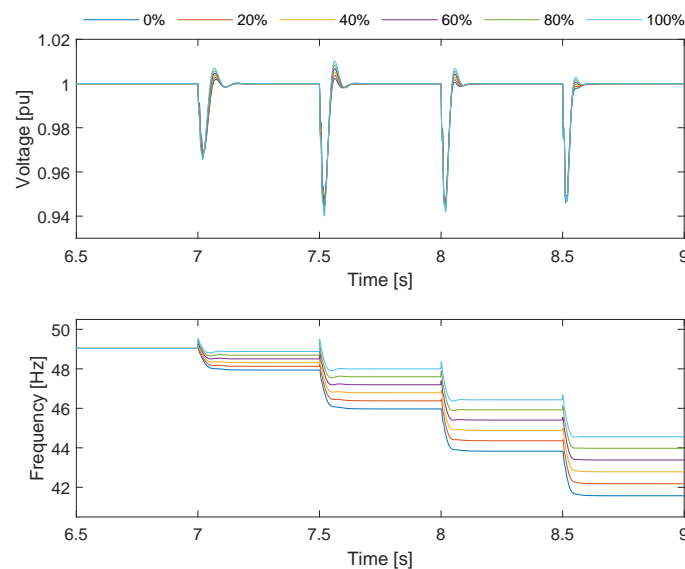

Figure 16. Voltage and frequency at the PCC during block loading for the different GFM penetrations (from 0% to 100%) without frequency control for the anchor scenario.

These results were unsatisfactory and thus the designed supervisory frequency support controller was switched on during the energisation for the anchor scenario. Results may be seen in Figure 17. This approach results in an increment in the active power reference for both controllers, ensuring that more power is injected to maintain the desired frequency and facilitate recovery from a dip following load energisation. It may be seen that this strategy mitigated the frequency deviation and the results are satisfactory for all GFM penetrations.
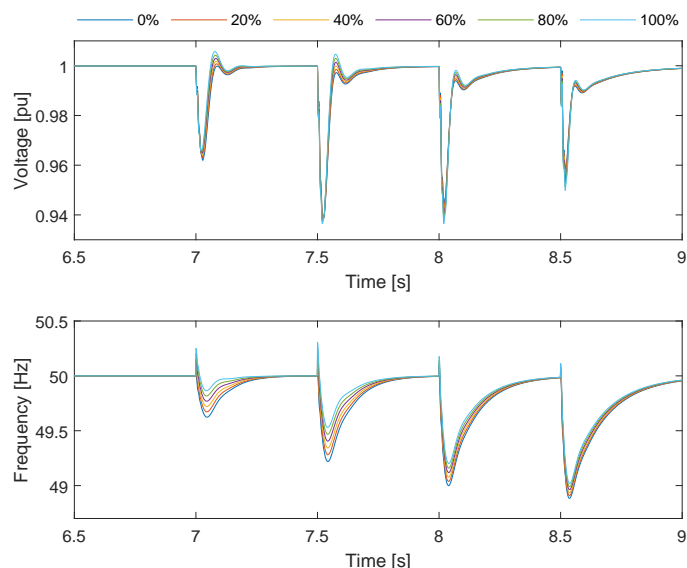

Figure 17. Voltage and frequency at the PCC during block loading for the different GFM penetrations (from 0% to 100%) with frequency control for the anchor scenario.

5.3. Discussion

Tables 5 and 6 display the final results with regards to the fulfillment of the requirements for the different GFM penetration percentages for both top-up and anchor generation, respectively. From these tables, it can be seen that all the requirements were met for all GFM penetrations.

Table 5. Top-up generation—results of EMT simulations for different GFM penetrations.

No.	0%	20%	40%	60%	80%	100%
1	✓	✓	✓	✓	✓	✓
2 f_{max}	50	50.05	50.11	50.16	50.22	50.27
2 f_{min}	49.93	49.96	49.98	49.99	50.00	50.00
3 V_{max}	1.00	1.00	1.00	1.00	1.00	1.00
3 V_{min}	0.992	0.991	0.990	0.989	0.988	0.987
4	✓	✓	✓	✓	✓	✓
5	✓	✓	✓	✓	✓	✓

Table 6. Anchor generation —results of EMT simulations for different GFM penetrations.

No.	0%	20%	40%	60%	80%	100%
1	✓	✓	✓	✓	✓	✓
2 f_{max}	50	50.06	50.12	50.18	50.25	50.31
2 f_{min}	48.88	48.91	48.94	48.96	48.99	49.02
3 V_{max}	1.00	1.00	1.00	1.00	1.00	1.00
3 V_{min}	0.939	0.938	0.938	0.937	0.937	0.936
4	✓	✓	✓	✓	✓	✓
5	✓	✓	✓	✓	✓	✓

6. Grid-Forming Penetration—Small-Signal Stability Analysis

A small-signal analysis was performed to analyse the overall stability of the power system, which includes both GFL and GFM aggregated wind farms connected to the power system. The aim of this study was to determine the best percentage of GFM penetration that offers enhanced stability and robustness during the block loading process. This study was performed for both anchor and top-up scenarios.

For this purpose, and just like for the EMT analysis displayed earlier, GFM penetration was varied from 0% to 100% in steps of 20%, and the RC load (R_{ld} and C_{ld}) was adjusted according to the provided active and reactive power values. An explanation on the computation of these parameters is available in Appendix A.

This section explains the linearisation process of the system, as well as its validation, and then stability results for both anchor and top-up and for the different steps of block loading are expanded in terms of disk margins.

6.1. Model Linearisation

The one-line diagram seen in Figure 8 was the baseline utilized for this study. The BESS was only used for WT energisation purposes and thus was removed, and the model utilized for small-signal studies may be seen in Figure 18. This model serves both top-up and anchor generation: for the top-up study, the grid, which is represented here as a Thevenin equivalent with R_p, L_p and the voltage source V_g, is connected; for the anchor scenario, the Thevenin circuit is removed.
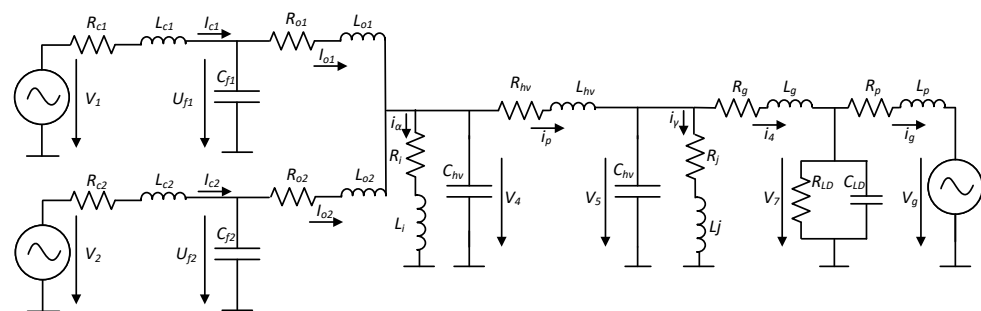

Figure 18. GFM and GFL converters forming the aggregated wind farms and power system for SSM analysis.

The state-space model, with respect to the aggregated wind farms (considering both grid-forming and grid-following converters), and the rest of the power system, from the offshore PCC to the electrical loads, may be seen in Appendix B. The difference between the top-up and anchor state space matrices is that of A_{PS}, B_{PS}, C_{PS} and D_{PS} and the wind farm matrices, represented as A_{WF}, B_{WF}, C_{WF} and D_{WF}, remain the same. Essentially, and looking at Figure 18, for the anchor analysis, the i_g current (represented in the synchronous frame as i_{gq} and i_{gd}) which flows through the grid Thevenin equivalent and the voltage source V_g (represented in the synchronous frame as v_{gq} and v_{gd}) are removed, reducing the overall size of the state space matrices.

The controllers utilized, and represented in Figure 2, were also linearised. The process of linearisation of these units is shown in Figure 19. Each component of both controllers was linearised as an independent system with a state-space representation, and then all of these components were connected depending on their inputs and outputs. As an example, it is described below how the inner loop controller was linearised and then the same approach can be used for all the other modules.

The equation that describes the inner loop controller may be seen in Equation (6). Following this and Figure 2, the state-space model that characterises this controller is the following.

$$\dot{x}_{cc} = A_{cc}x_{cc} + B_{cc}u_{cc} \tag{17}$$

$$y_{cc} = C_{cc}x_{cc} + D_{cc}u_{cc} \tag{18}$$

where the state-space matrices are defined as:

$$A_{cc} = 0$$

$$B_{cc} = \begin{bmatrix} -1 & 0 & 1 & 0 & 0 & 0 \\ 0 & -1 & 0 & 1 & 0 & 0 \end{bmatrix}$$

$$C_{cc} = \begin{bmatrix} k_{i,cc} & 0 \\ 0 & k_{i,cc} \end{bmatrix}$$

$$D_{cc} = \begin{bmatrix} -k_{p,cc} & 0 & k_{p,cc} & -\omega L_c & 1 & 0 \\ 0 & -k_{p,cc} & \omega L_c & k_{p,cc} & 0 & 0 \end{bmatrix}$$

The inputs, u_{cc} and outputs, y_{cc} of the inner loop current controller are the following:

$$u_{cc} = \begin{bmatrix} i_{lq}^* & i_{ld}^* & i_{c2q}' & i_{c2d}' & \Delta u_{f2q}' & \Delta u_{f2d}' \end{bmatrix} \tag{19}$$

$$y_{cc} = \begin{bmatrix} v_{2q} & v_{2d} \end{bmatrix} \tag{20}$$

It can be seen from the figure that both the GFM and GFL units use the voltage ΔV_{4qd} and the current $I_{\alpha qd}$ as inputs. These quantities are transformed from the conventional *abc* frame into the *qd*0 frame and then used in the different modules that can be seen in the figure.
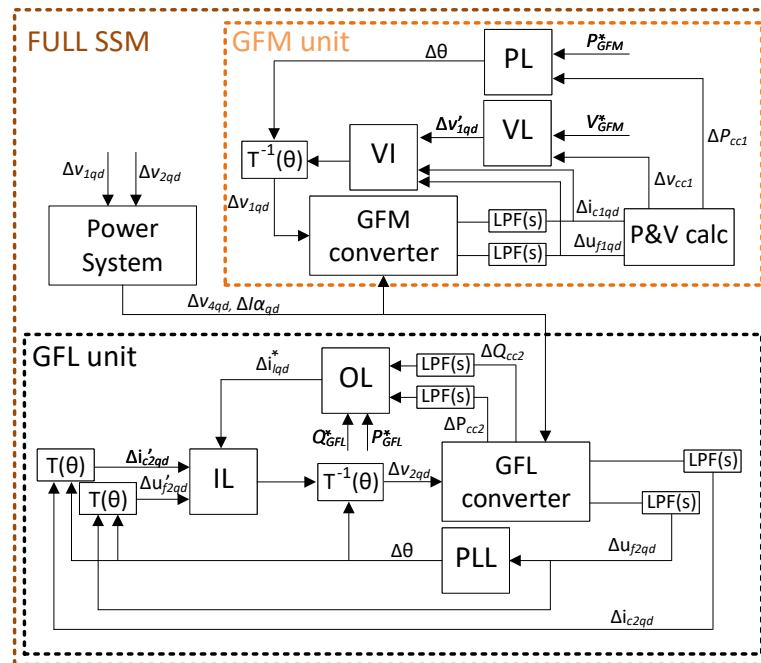

Figure 19. Scheme of the linearised system (SSM) with both GFM and GFL aggregated wind farms and controllers and power system.

6.2. Small-Signal Model Validation

After developing the SSM, the first step was to validate this model by matching it against the EMT model. For this purpose, three power steps of 0.01 pu were applied to both the EMT and SSM. This may be seen in Figure 20 for both the GFL and GFM converters. From these figures, it is evident that the SSM consistently follows the EMT line, demonstrating that the SSM is an accurate representation of the EMT simulations.
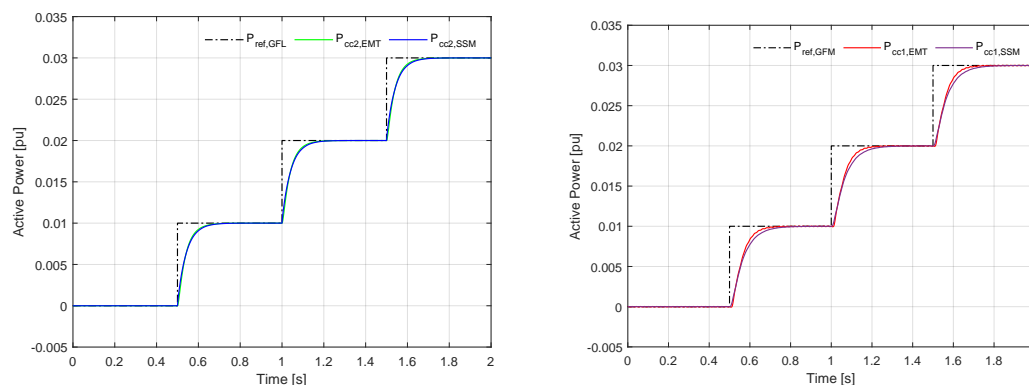

Figure 20. SSM validation for both GFL (**left**) and GFM (**right**) converter controllers: Active power reference, $P_{ref,GFL}$ and $P_{ref,GFM}$; PCC active power from EMT model, $P_{cc2,EMT}$ and $P_{cc1,EMT}$; and PCC active power from SSM, $P_{cc2,SSM}$ and $P_{cc1,SSM}$.

6.3. Stability Analysis

The small-signal stability was analysed using disk margins (DMs), which quantify the stability and robustness of a closed-loop system by multiplying the open-loop system "L" by a factor "f". Although a brief introduction on disk margins will be given in this section, stability via disk margins was already used in several studies [37,38,60–62]. There are two different analyses that may be applied. The first one is called loop-at-a-time and introduces a perturbation "f" in a single channel (input or output) while holding the other channels fixed. However, this approach may be optimistic as it fails to capture the effects of simultaneous perturbations. For this, multi-loop DMs are used that apply in different channels different perturbations, and hence a matrix of perturbations "F" is considered.

The multi-loop input/output disk margin is a single number, α, which defines the largest disk of perturbations for which the closed loop system is stable [60]. Therefore, introducing factors in all the channels simultaneously outputs the worst case scenario of a system. Thus, to assess how stable and robust the studied systems were, the parameter α was used. If $\alpha = 0$, the system has no room for any uncertainty. The further away it goes from 0, the more stable the system becomes.

This analysis was performed for both anchor and top-up scenarios and for different steps of block loading using the local network demand data previously used for the EMT simulations.

The analysis process was as follows: For both anchor and top-up scenarios, EMT simulations were conducted for different GFM penetrations (from 0% to 100%) and various loads (P1, P2, P3, P4). From these simulations, the initial conditions for the state space models were obtained. Then, the small-signal model analysis was performed, retrieving DMs, gain, and phase margins for each case. The stability and robustness were compared for each GFM penetration and for both top-up and anchor scenarios based on these results.

Figure 21 shows the DMs for the top-up scenario. The x-axis represents the GFM penetration, and the y-axis represents the active power on the load. The results indicate that for all GFM penetrations and active power demands, the system remains stable (DM > 0). Additionally, from P1 to P4, the DM increases, suggesting that the system becomes more

stable with more loads connected. This increased stability occurs because the added loads provide more damping, which reduces the amplitude of oscillations and helps stabilize the system after a disturbance. Additionally, connecting more loads increases the overall inertia of the system, allowing it to withstand and absorb disturbances without experiencing large fluctuations in frequency or voltage.

The highest DM values are observed at 40% and 60% GFM penetration, with robustness decreasing at higher or lower percentages. Although margins differ for each GFM penetration and active power load, the variations are not significant.

The results for the anchor scenario, shown in Figure 22, differ from those of the top-up scenario. Firstly, it can be seen that all DMs are lower. This is due to the fact that in the top-up scenario, the system is connected to an external grid, which, as previously mentioned, is represented as a voltage Thevenin equivalent. The presence of this external grid increases stability margins due to the external grid support, as this source acts as a large stable voltage source and hence helps in absorbing possible disturbances and reducing the impact of oscillations. Furthermore, this voltage source also offers more inertia and enhanced damping.
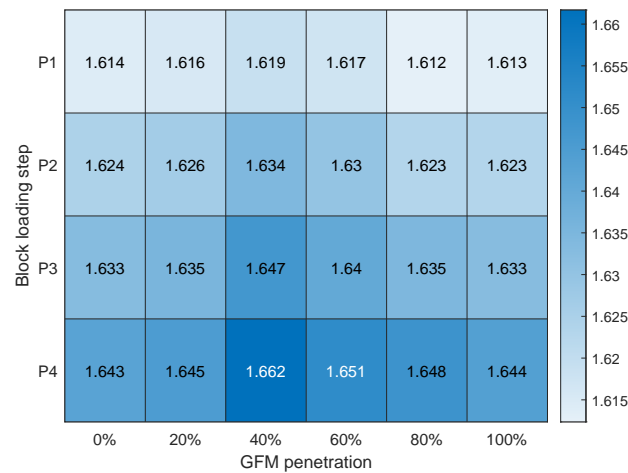

Figure 21. DM results for the top-up scenario.

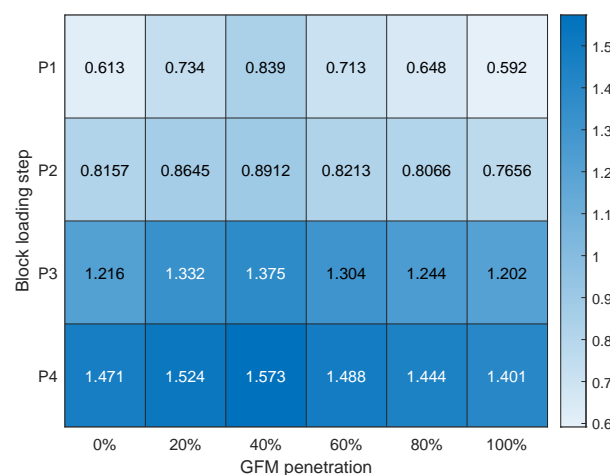
Figure 22. DM results for the anchor scenario.

Similar to the top-up scenario, increasing connected loads leads to higher DMs and greater system robustness. However, this increase is more pronounced in the anchor scenario. There is also a significant difference in margins between different GFM penetration percentages. The highest stability DM occurs at 40% penetration, followed by 20% and

then 60%. Without the Thevenin equivalent of an electrical grid connected (network representation), the system has lower overall margins, and a slightly lower percentage of GFM penetration is preferred. In the absence of such an external grid, the system needs a sufficient number of GFM converters to provide good robustness and stability. A percentage between 20% and 40% was seen to ensure enough inertia and control to manage the system without overburdening it with too many GFM converters. Above 40% GFM converters, too many GFM converters can lead to over-compensation, causing control issues and reducing overall stability.

In conclusion, the stability analysis revealed that the margins are larger in the top-up scenario as the system is connected to an external grid. This connection provides additional support, increased inertia, enhanced damping, and improved voltage and frequency regulation, all of which contribute to greater stability. In the anchor scenario, a preferred percentage of 20% to 40% GFM converters is required. This range ensures a balance of inertia and control, avoiding over-compensation that could lead to lower stability. Conversely, in the top-up scenario, the preferred percentage of GFM converters is between 40% and 60% due to the additional support from the external grid. This support allows the system to handle a higher percentage of GFM converters, meeting the increased inertia requirement and maintaining stability under various load conditions.

7. Conclusions

This study provided an analysis of the potential for OWPPs to contribute to PSR in the UK, particularly in the context of the shift from fossil fuels to inverter-based RESs. The findings of the SIF BLADE project demonstrate that OWPPs, when equipped with GFM control strategies, can support PSR by meeting technical requirements.

Given the transition away from fossil fuels, it is necessary to explore the capability of inverter-based RESs in providing essential grid services like PSR. The SIF BLADE project was initiated to assess the feasibility of PSR from OWPPs. A series of comprehensive studies was conducted to evaluate this potential.

A steady-state analysis was performed to assess the OWPP's ability to meet local network demands for active and reactive power. This study confirmed that OWPPs could fulfil these demands with minimal adjustments such as tuning of controllers or even when accounting for variations in reactive power compensation and cable lengths. These findings were aligned with industry benchmarks and partner data, demonstrating that OWPPs can maintain performance under different steady-state conditions.

In the EMT studies, various GFM penetration levels (ranging from 0% to 100% in 20% increments) were tested against the technical standards set by the NGESO. The EMT analysis confirmed that all tested levels of GFM penetration successfully met the required standards, proving the feasibility of OWPPs to comply with grid requirements under different levels of GFM integration.

The small-signal analysis aimed to determine the optimal GFM penetration levels for PSR. It was found that for top-up generation scenarios, a GFM penetration between 40% and 60% offered the highest stability and robustness with significant margins. Conversely, for anchor generation scenarios, a lower penetration range of 20% to 40% was recommended to ensure optimal performance.

The external supervisory controller, integrated with both GFM and GFL loops, mitigated frequency drops during load restoration. This controller adjusts active power references in response to frequency deviations, functioning similarly to a governor in synchronous generators. The power adjustment strategy was designed to distribute the load between GFM and GFL controllers proportionally to the GFM penetration level, ensuring a balanced and optimized response.

While these results underscore the capability of OWPPs to serve as reliable resource for PSR, the study also highlighted certain limitations. The use of an aggregated OWPP model presented challenges, particularly in synchronizing GFM and GFL units. Future work should focus on developing a wind turbine-specific model to address these limitations and explore transient effects arising from array cables and wind turbine transformers, which were not considered in this study. Moreover, these studies involved GFM WTs, an emerging technology that requires further validation and cost assessment.

The specifically developed wind turbine model will be validated through the hardware-in-the-loop (HIL) test, which offers a realistic, controlled, and easily reconfigurable test environment to test whether the performance of the laboratory HIL wind turbine simulator aligns with any specific existing turbine. Given the importance of speed and accuracy in control for power system restoration, the feasibility of the GFM WT will be evaluated by implementation of the GFM controller connected to a virtual OWPP via HIL. Furthermore, future work will also include transient performance analysis considering array cables, wind turbine transformers, and the interactions in the OWPP between GFM WT and GFL WT controllers by HIL simulation.

Furthermore, while this study highlights the technical feasibility of OWPPs in providing PSR services, future work should address the economic and regulatory aspects. A cost analysis for retrofitting existing RESs for grid services and an evaluation of legal requirements for new projects could provide valuable insights to guide practical implementation and policy development.

It should also be mentioned that the availability of wind resources is a critical factor in assessing the feasibility of using OWPPs for BS services. While this study does not include a detailed risk assessment of wind availability, such an analysis has been conducted and will be presented in a subsequent publication.

In conclusion, this research has provided insights into the role that OWPPs can play in PSR as the energy sector transitions to low-carbon technologies. The findings demonstrate that OWPPs, with optimized GFM and GFL integration, can enhance the resilience and stability of power systems during restoration. Future research should continue to refine these strategies and optimize the deployment of GFM and self-start units within OWPPs to fully realize their potential in providing essential grid services.

Abbreviations

The following abbreviations are used in this manuscript:

APS	Auxiliary power supply
BESS	Battery energy storage system
BS	Black start
BSU	Black start unit
BRK	Breaker
DG	Diesel generator
DFIG	Doubly-fed induction generator
DM	Disk margin
GFL	Grid-following
GFM	Grid-forming
HIL	Hardware-in-the-loop
HVAC	High-voltage alternating current
NBSU	Non-black-start unit
NGESO	National Grid Electricity System Operator
OWPP	Offshore wind power plant
PCC	Point of common coupling
PIR	Pre-insertion resistor
PLL	Phase-locked loop
PMSG	Permanent magnet synchronous generators
POW	Point on wave
PSR	Power system restoration
RES	Renewable energy source
SIF	Strategic Innovation Fund
SVCC	Standard vector current control
TSO	Transmission system operator
WT	Wind turbine

Appendix A

This section contains the parameters used in both the EMT and small-signal models. Most of the parameters remain the same for all the studies performed. However, as shown in Table A2, the values of the load resistor and capacitor changed throughout the study to accommodate four block loading active and reactive power steps.

Since the values of active and reactive power at the load were provided (P1 to P4 and Q1 to Q4), and considering a three-phase balanced system, R_{ld} and C_{ld} were computed as follows:

$$Rld = \frac{V_7^2}{P_{ld}} \tag{A1}$$

where V_7 is the voltage at the load terminals, as shown in Figure 18, and P_{ld} is the active power demanded by the load.

$$C_{ld} = \frac{Q_{ld}}{2\pi f V_7^2} \tag{A2}$$

where Q_{ld} is the capacitive reactive power consumed by the load.

Regarding the shunt compensations used to compensate for the reactive power excess due to the high capacitance of the HVAC submarine cable, both onshore and offshore, and after determining exactly how much reactive power needed to be compensated, the inductance per phase was computed as follows:

$$Li, j = \frac{V_{4,6}^2}{2\pi f Q_{4,6}} \tag{A3}$$

where $V_{4,6}$ is the voltage at the terminals of the offshore or onshore shunt compensations, and $Q_{4,6}$ is the reactive power measured at the same location. The reactive power to be compensated was chosen to enable a power factor close to unity at the offshore PCC and to maintain a voltage level within the 0.9 pu and 1.1 pu range established by the TSO.

Table A1. Power system parameters.

Parameter	Value	Unit
S_{base}	350	MVA
Z_{base}	151	Ω
E_1, E_2	66	kV
R_c	0.1245	Ω
L_c	3.1693	mH
C_f	1.2788	mF
R_g	0.2489	Ω
L_g	7.9232	mH/km
R_{hv}	0.0216	Ω/km
L_{hv}	0.44	mH/km
C_{hv}	1.3518	μF/km
R_o	0.02	Ω
L_o	0.2	mH/km
R_p	0.02	Ω
L_p	0.2	mH/km
L_i	0.2495	mH
L_j	0.3742	mH

Table A2. (P,Q) pairs, R_{LD}, and CLD for local network studies.

Step	P (MW)	Q (MVAr)	R_{LD} (Ω)	C_{LD} (μF)
(P_1, Q_1)	70	0.40	745	0.0241
(P_2, Q_2)	156	8	339	0.4814
(P_3, Q_3)	206	21	257	1.2636
(P_4, Q_4)	241	31	220	1.8653

Table A3. Offshore transformer parameters.

Parameter	Value	Unit
Apparent power	2.3	MVA
Frequency	50	Hz
V_1	6.6	kV
V_2	230	kV
R_1	0.002	pu
L_1	0.08	pu
R_2	0.002	pu
L_2	0.08	pu
R_m	500	pu
Saturation pairs (i, ϕ)	[0,0; 0,0.9; 0.0024,1.2; 1,1.52]	pu
Initial flux (a, b, c)	[0.8, 0, -0.8]	pu

Table A4. Grid-forming converter controller parameters.

Parameter	Value
m_p	1.5×10^{-8}
m_i	0.9×10^{-7}
$k_{p,VCC}$	1.2
$k_{i,VCC}$	10
R_v	0.38
L_v	1×10^{-3}

Table A5. Grid-following converter controller parameters.

Parameter	Value
$k_{p,PLL}$	0.0024
$k_{i,PLL}$	0.5256
τ_{il}	2×10^{-3}
$k_{p,il}$	1.5846
$k_{i,il}$	62.2286
$k_{p,PC}$	8.02×10^{-7}
$k_{i,PC}$	2.862×10^{-4}
$k_{p,QC}$	6.416×10^{-6}
$k_{i,QC}$	9.54×10^{-4}

Appendix B

This appendix includes the matrices, state space vectors, and inputs that were used for both the aggregated wind farm and power system for the linear time-invariant model developed to study small-signal stability. A_{WF}, B_{WF}, $\dot{x}_{WF}$, and u_{WF} form the state-space representation of the aggregated wind farms with both grid-forming and grid-following converters. A_{PS}, B_{PS}, $\dot{x}_{PS}$, and u_{PS} form the state-space representation of the power system, from the offshore PCC to the electrical grid and RC load.

$$
A_{WF} = \begin{bmatrix}
-\frac{R_c}{L_c} & -\omega & -\frac{1}{L_c} & 0 & 0 & 0 & 0 & 0 & 0 & 0 & 0 & 0 \\
\omega & -\frac{R_c}{L_c} & 0 & -\frac{1}{L_c} & 0 & 0 & 0 & 0 & 0 & 0 & 0 & 0 \\
\frac{1}{C_f} & 0 & 0 & -\omega & -\frac{1}{C_f} & 0 & 0 & 0 & 0 & 0 & 0 & 0 \\
0 & \frac{1}{C_f} & \omega & 0 & 0 & -\frac{1}{C_f} & 0 & 0 & 0 & 0 & 0 & 0 \\
0 & 0 & \frac{1}{L_o} & 0 & -\frac{R_o}{L_o} & -\omega & 0 & 0 & 0 & 0 & 0 & 0 \\
0 & 0 & 0 & \frac{1}{L_o} & \omega & -\frac{R_o}{L_o} & 0 & 0 & 0 & 0 & 0 & 0 \\
0 & 0 & 0 & 0 & 0 & 0 & -\frac{R_c}{L_c} & -\omega & \frac{1}{L_c} & 0 & 0 & 0 \\
0 & 0 & 0 & 0 & 0 & 0 & \omega & -\frac{R_c}{L_c} & 0 & \frac{1}{L_c} & 0 & 0 \\
0 & 0 & 0 & 0 & 0 & 0 & -\frac{1}{C_f} & 0 & 0 & -\omega & \frac{1}{C_f} & 0 \\
0 & 0 & 0 & 0 & 0 & 0 & 0 & -\frac{1}{C_f} & \omega & 0 & 0 & \frac{1}{C_f} \\
0 & 0 & 0 & 0 & 0 & 0 & 0 & 0 & -\frac{1}{L_o} & 0 & -\frac{R_o}{L_o} & -\omega \\
0 & 0 & 0 & 0 & 0 & 0 & 0 & 0 & 0 & -\frac{1}{L_o} & \omega & -\frac{R_o}{L_o}
\end{bmatrix}
$$

$$B_{WF} = \begin{bmatrix} \frac{1}{L_c} & 0 & 0 & 0 & 0 & 0 \\ 0 & \frac{1}{L_c} & 0 & 0 & 0 & 0 \\ 0 & 0 & 0 & 0 & 0 & 0 \\ 0 & 0 & 0 & 0 & 0 & 0 \\ 0 & 0 & 0 & 0 & -\frac{1}{L_o} & 0 \\ 0 & 0 & 0 & 0 & 0 & -\frac{1}{L_o} \\ 0 & 0 & -\frac{1}{L_c} & 0 & 0 & 0 \\ 0 & 0 & 0 & -\frac{1}{L_c} & 0 & 0 \\ 0 & 0 & 0 & 0 & 0 & 0 \\ 0 & 0 & 0 & 0 & 0 & 0 \\ 0 & 0 & 0 & 0 & \frac{1}{L_o} & 0 \\ 0 & 0 & 0 & 0 & 0 & \frac{1}{L_o} \end{bmatrix}$$

$$\dot{x}_{WF} = \begin{bmatrix} i_{c1q} & i_{c1d} & u_{f1q} & u_{f1d} & i_{o1q} & i_{o1d} & i_{c2q} & i_{c2d} & u_{f2q} & u_{f2d} & i_{o2q} & i_{o2d} \end{bmatrix}$$

$$u_{WF} = \begin{bmatrix} v_{1q} & v_{1d} & v_{2q} & v_{2d} & v_{4q} & v_{4d} \end{bmatrix}$$

$$A_{PS} = \begin{bmatrix} 0 & -\omega & \frac{1}{L_i} & 0 & 0 & 0 & 0 & 0 & 0 & 0 & 0 & 0 & 0 & 0 & 0 & 0 \\ \omega & 0 & 0 & \frac{1}{L_i} & 0 & 0 & 0 & 0 & 0 & 0 & 0 & 0 & 0 & 0 & 0 & 0 \\ -\frac{1}{C_{HV}} & 0 & 0 & -\omega & -\frac{1}{C_{HV}} & 0 & 0 & 0 & 0 & 0 & 0 & 0 & 0 & 0 & 0 & 0 \\ 0 & -\frac{1}{C_{HV}} & \omega & 0 & 0 & -\frac{1}{C_{HV}} & 0 & 0 & 0 & 0 & 0 & 0 & 0 & 0 & 0 & 0 \\ 0 & 0 & \frac{1}{L_{HV}} & 0 & -\frac{R_{HV}}{L_{HV}} & -\omega & -\frac{1}{L_{HV}} & 0 & 0 & 0 & 0 & 0 & 0 & 0 & 0 & 0 \\ 0 & 0 & 0 & \frac{1}{L_{HV}} & \omega & -\frac{R_{HV}}{L_{HV}} & 0 & -\frac{1}{L_{HV}} & 0 & 0 & 0 & 0 & 0 & 0 & 0 & 0 \\ 0 & 0 & 0 & 0 & \frac{1}{C_{HV}} & 0 & 0 & -\omega & -\frac{1}{C_{HV}} & 0 & -\frac{1}{C_{HV}} & 0 & 0 & 0 & 0 & 0 \\ 0 & 0 & 0 & 0 & 0 & \frac{1}{C_{HV}} & \omega & 0 & 0 & -\frac{1}{C_{HV}} & 0 & -\frac{1}{C_{HV}} & 0 & 0 & 0 & 0 \\ 0 & 0 & 0 & 0 & 0 & 0 & \frac{1}{L_j} & 0 & 0 & -\omega & 0 & 0 & 0 & 0 & 0 & 0 \\ 0 & 0 & 0 & 0 & 0 & 0 & 0 & \frac{1}{L_j} & \omega & 0 & 0 & 0 & 0 & 0 & 0 & 0 \\ 0 & 0 & 0 & 0 & 0 & 0 & \frac{1}{L_g} & 0 & 0 & -\frac{R_g}{L_g} & -\omega & -\frac{1}{L_g} & 0 & 0 & 0 & 0 \\ 0 & 0 & 0 & 0 & 0 & 0 & 0 & \frac{1}{L_g} & 0 & \omega & -\frac{R_g}{L_g} & 0 & -\frac{1}{L_g} & 0 & 0 & 0 \\ 0 & 0 & 0 & 0 & 0 & 0 & 0 & 0 & 0 & \frac{1}{C_{ld}} & 0 & -\frac{1}{C_{ld}\cdot R_{ld}} & -\omega & -\frac{1}{C_{ld}} & 0 & 0 \\ 0 & 0 & 0 & 0 & 0 & 0 & 0 & 0 & 0 & 0 & \frac{1}{C_{ld}} & -\frac{1}{C_{ld}\cdot R_{ld}} & \omega & 0 & -\frac{1}{C_{ld}} & 0 \\ 0 & 0 & 0 & 0 & 0 & 0 & 0 & 0 & 0 & 0 & 0 & \frac{1}{L_p} & 0 & -\frac{R_p}{L_p} & -\omega & 0 \\ 0 & 0 & 0 & 0 & 0 & 0 & 0 & 0 & 0 & 0 & 0 & 0 & \frac{1}{L_p} & \omega & -\frac{R_p}{L_p} \end{bmatrix}$$

$$B_{PS} = \begin{bmatrix} 0 & 0 & 0 & 0 & 0 & 0 \\ 0 & 0 & 0 & 0 & 0 & 0 \\ \frac{1}{C_{HV}} & 0 & -\frac{1}{C_{HV}} & 0 & 0 & 0 \\ 0 & \frac{1}{C_{HV}} & 0 & -\frac{1}{C_{HV}} & 0 & 0 \\ 0 & 0 & 0 & 0 & 0 & 0 \\ 0 & 0 & 0 & 0 & 0 & 0 \\ 0 & 0 & 0 & 0 & 0 & 0 \\ 0 & 0 & 0 & 0 & 0 & 0 \\ 0 & 0 & 0 & 0 & 0 & 0 \\ 0 & 0 & 0 & 0 & 0 & 0 \\ 0 & 0 & 0 & 0 & 0 & 0 \\ 0 & 0 & 0 & 0 & 0 & 0 \\ 0 & 0 & 0 & 0 & -\frac{1}{L_p} & 0 \\ 0 & 0 & 0 & 0 & 0 & -\frac{1}{L_p} \end{bmatrix}$$

$$\dot{x}_{PS} = \begin{bmatrix} i_{\alpha,q} & i_{\alpha,d} & v_{4q} & v_{4d} & i_{2q} & i_{2d} & v_{5q} & v_{5d} & i_{\gamma,q} & i_{\gamma,d} & i_{4q} & i_{4d} & v_{7q} & v_{7d} & i_{gq} & i_{gd} \end{bmatrix}$$

$$u_{PS} = \begin{bmatrix} i_{o1q} & i_{o1d} & i_{o2q} & i_{o2d} & v_{gq} & v_{gd} \end{bmatrix}$$

References

1. Hassan, Q.; Viktor, P.J.; Al-Musawi, T.; Mahmood Ali, B.; Algburi, S.; Alzoubi, H.M.; Khudhair Al-Jiboory, A.; Zuhair Sameen, A.; Salman, H.M.; Jaszczur, M. The renewable energy role in the global energy Transformations. *Renew. Energy Focus* **2024**, *48*, 100545. [CrossRef]

2. Letcher, T. *Wind Energy Engineering: A Handbook for Onshore and Offshore Wind Turbines*; Elsevier Inc.: Amsterdam, The Netherlands, 2023. [CrossRef]

3. Jain, H.; Seo, G.S.; Lockhart, E.; Gevorgian, V.; Kroposki, B. Blackstart of power grids with inverter-based resources. In Proceedings of the IEEE Power and Energy Society General Meeting, Montreal, QC, Canada, 2–6 August 2020. [CrossRef]

4. Teng, W.; Wang, H.; Jia, Y. Construction and control strategy research of black start unit containing wind farm. In Proceedings of the IEEE Region 10 Annual International Conference, Proceedings/TENCON, Singapore, 22–25 November 2016. [CrossRef]

5. Giampieri, A.; Ling-Chin, J.; Roskilly, A.P. Techno-economic assessment of offshore wind-to-hydrogen scenarios: A UK case study. *Int. J. Hydrogen Energy* **2023**, *52*, 589–617. [CrossRef]

6. PROMOTioN—Progress on Meshed HVDC Offshore Transmission Networks. Deliverable 3.7: Compliance Evaluation Results Using Simulations. Technical Report, PROMOTioN—Progress on Meshed HVDC Offshore Transmission Networks, 2020. Available online: http://www.promotion-offshore.net/fileadmin/PDFs/D3.7_Compliance_evaluation_results_using_simulations.pdf (accessed on 11 January 2025).

7. PROMOTioN —Progress on Meshed HVDC Offshore Transmission Networks. Deliverable 2.4 Requirement Recommendations to Adapt and Extend Existing Grid Codes. Technical Report, 2020. Available online: https://ec.europa.eu/research/participants/documents/downloadPublic?documentIds=080166e5c9d8102b&appId=PPGMS (accessed on 11 January 2025).

8. National Grid ESO. Black Startfrom Non-Traditional Generation Technologies. Technical Report, 2019. Available online: https://www.neso.energy/document/148201/download (accessed on 11 January 2025).

9. Carbon Trust. Black Start Demonstration from Offshore Wind (SIF BLADE). 2023. Available online: https://www.carbontrust.com/our-work-and-impact/impact-stories/large-scale-rd-projects-offshore-wind/black-start-demonstration-from-offshore-wind-sif-blade (accessed on 11 January 2025).

10. ESO, N.G. GC0156 : Facilitating the Implementation of the Electricity System Restoration Standard. 2023. Available online: https://www.neso.energy/industry-information/codes/gc/modifications/gc0156-facilitating-implementation-electricity-system-restoration-standard (accessed on 11 January 2025).

11. Su, J.; Dehghanian, P.; Nazemi, M.; Wang, B. Distributed Wind Power Resources for Enhanced Power Grid Resilience. In Proceedings of the 51st North American Power Symposium, NAPS 2019, Wichita, KS, USA, 13–15 October 2019; pp. 1–6. [CrossRef]

12. Patsakis, G.; Rajan, D.; Aravena, I.; Rios, J.; Oren, S. Optimal black start allocation for power system restoration. *IEEE Trans. Power Syst.* **2018**, *33*, 6766–6776. [CrossRef]

13. Ganganath, N.; Wang, J.V.; Xu, X.; Cheng, C.T.; Tse, C.K. Agglomerative clustering-based network partitioning for parallel power system restoration. *IEEE Trans. Ind. Inform.* **2018**, *14*, 3325–3333. [CrossRef]

14. Khoshkhoo, H.; Khalilifar, M.; Shahrtash, S.M. Survey of Power System Restoration Documents Issued from 2016 to 2021. *Int. Trans. Electr. Energy Syst.* **2022**, *2022*, 1754013. [CrossRef]

15. Feltes, J.W.; Grande-Moran, C. Black start studies for system restoration. In Proceedings of the IEEE Power and Energy Society 2008 General Meeting: Conversion and Delivery of Electrical Energy in the 21st Century, PES, Pittsburgh, PA, USA, 20–24 July 2008; pp. 1–8. [CrossRef]

16. Udoakah, Y.O.; Khalaf, S.; Cipcigan, L. Blackout and Black Start Analysis for Improved Power System Resilience: The African Experience. In Proceedings of the 2020 IEEE PES/IAS PowerAfrica, PowerAfrica 2020, Online, 25–28 August 2020; pp. 1–5. [CrossRef]

17. Liu, Y.; Fan, R.; Terzija, V. Power system restoration: A literature review from 2006 to 2016. *J. Mod. Power Syst. Clean Energy* **2016**, *4*, 332–341. [CrossRef]

18. Oliveira, L.W.; Oliveira, E.J.; Silva, I.C.; Gomes, F.V.; Borges, T.T.; Marcato, A.L.; Oliveira, A.R. Optimal restoration of power distribution system through particle swarm optimization. In Proceedings of the 2015 IEEE Eindhoven PowerTech, PowerTech 2015, Eindhoven, The Netherlands, 29 June–2 July 2015. [CrossRef]

19. Pagnani, D.; Blaabjerg, F.; Bak, C.L.; Da Silva, F.M.F.; Kocewiak, Ł.H.; Hjerrild, J. Offshore wind farm black start service integration: Review and outlook of ongoing research. *Energies* **2020**, *13*, 6286. [CrossRef]

20. Pagnam, D.; Kocewiak, L.H.; Hjerrild, J.; Blaabjerg, F.; Bak, C.L. Overview of Black Start Provision by Offshore Wind Farms. In Proceedings of the IECON Proceedings (Industrial Electronics Conference), Singapore, 18–21 October 2020; pp. 1892–1898. [CrossRef]

21. Jain, A.; Sakamuri, J.N.; Das, K.; Göksu, Ö.; Cutululis, N.A. Functional Requirements for Blackstart and Power System Restoration from Wind Power Plants. In Proceedings of the 2nd International Conference on Large-Scale Grid Integration of Renewable Energy in India, New Delhi, India, 4–6 September 2019. [CrossRef]

22. European Commission. Commission Regulation (EU) 2016/1447 of 26 August 2016: Establishing a Network Code on Requirements for Grid Connection of High Voltage Direct Current Systems and Direct Current-Connected Power Park Modules. *Off. J. Eur. Union* **2016**, *59*, L 241.

23. Göksu, Ö.; Saborío-Romano, O.; Cutululis, N.A.; Sørensen, P. Black Start and Island Operation Capabilities of Wind Power Plants. In Proceedings of the 16th Wind Integration Workshop, 2017; pp. 25–27. Available online: https://backend.orbit.dtu.dk/ws/portalfiles/portal/205667823/G_ksu_et_al._2017_Black_Start_and_Island_Operation_Capabilities_of_Wind_Power_Plants.pdf (accessed on 11 January 2025).

24. Teichmann, R.; Li, L.; Wang, C.; Yang, W. Method, Apparatus and Computer Program Product for Wind Turbine Start-Up and Operation Without Grid Power. U.S. Patent No. US7,394,166B2, 1 June 2008.

25. Yu, L.; Li, R.; Xu, L. Distributed PLL-Based Control of Offshore Wind Turbines Connected with Diode-Rectifier-Based HVDC Systems. *IEEE Trans. Power Deliv.* **2018**, *33*, 1328–1336. [CrossRef]

26. Egedal, P.; Kumar, S.; Nielsen, K.S. Black Start of Wind Turbine Devices. U.S. Patent 9,509,141, 29 November 2016. Available online: https://patents.justia.com/patent/9509141 .

27. Tee, J.Z.; Lim, I.L.H.; Zhou, K.; Anaya-Lara, O. Transient Stability Analysis of Offshore Wind with OG Platforms and an Energy Storage System. In Proceedings of the IEEE Power and Energy Society General Meeting, Montreal, QC, Canada, 2–6 August 2020; pp. 1–5. [CrossRef]

28. Chapaloglou, S.; Varagnolo, D.; Tedeschi, E. Techno-Economic Evaluation of the Sizing and Operation of Battery Storage for Isolated Oil and Gas Platforms with High Wind Power Penetration. In Proceedings of the IECON Proceedings (Industrial Electronics Conference), Lisbon, Portugal, 14–17 October 2019; pp. 4587–4592. [CrossRef]

29. Tee, J.Z.; Li Hong Lim, I.; Yang, J.; Choo, C.T.; Anaya-Lara, O.; Chui, C.K. Power system stability of offshore wind with an energy storage to electrify OG platform. In Proceedings of the IEEE Region 10 Annual International Conference, Proceedings/TENCON, Osaka, Japan, 16–19 November 2020; pp. 146–151. [CrossRef]

30. Adeyemo, A.A.; Tedeschi, E. Technology Suitability Assessment of Battery Energy Storage System for High-Energy Applications on Offshore Oil and Gas Platforms. *Energies* **2023**, *16*, 6490. [CrossRef]

31. Tee, J.Z. Development and Analysis of Hybrid Renewable Energy System for Offshore Oil and Gas Rigs. Ph.D. Thesis, University of Glasgow, Glasgow, Scotland, 2022. [CrossRef]

32. Huang, X.; Chen, Y. Hybrid Auxiliary Power Supply System for Offshore Wind Farm. *J. Physics Conf. Ser.* **2018**, *1102*, 012033. [CrossRef]

33. Chau, T.K.; Shenglong Yu, S.; Fernando, T.; Iu, H.H.C.; Small, M. An investigation of the impact of pv penetration and BESS capacity on islanded microgrids-a small-signal based analytical approach. In Proceedings of the IEEE International Conference on Industrial Technology, Melbourne, Australia, 13–15 February 2019; pp. 1679–1684. [CrossRef]

34. Lee, D.J.; Wang, L. Small-signal stability analysis of an autonomous hybrid renewable energy power generation/energy storage system part I: Time-domain simulations. *IEEE Trans. Energy Convers.* **2008**, *23*, 311–320. [CrossRef]

35. Abdelrahim, A.; Smailes, M.; Ahmed, K.; McKeever, P.; Egea-Alvarez, A. Modified grid forming converter controller with fault ride through capability without PLL or current loop. In Proceedings of the 18th Wind Integration Workshop, Dublin, Ireland, 16–18 October 2019; pp. 1–8.

36. Henderson, C.; Egea-Alvarez, A.; Kneuppel, T.; Yang, G.; Xu, L. Grid Strength Impedance Metric: An Alternative to SCR for Evaluating System Strength in Converter Dominated Systems. *IEEE Trans. Power Deliv.* **2024**, *39*, 386–396. [CrossRef]

37. Henderson, C.; Egea-Alvarez, A.; Xu, L. Analysis of multi-converter network impedance using MIMO stability criterion for multi-loop systems. *Electr. Power Syst. Res.* **2022**, *211*, 108542. [CrossRef]

38. Alves, R.; Egea-Àlvarez, A.; Knuppel, T. Grid forming and grid following comparison for an offshore wind farm connected via a HVAC cable. In Proceedings of the 21st Wind & Solar Integration Workshop (WIW 2022), The Hague, The Netherlands, 12–14 October 2022; pp. 9–16. [CrossRef]

39. Du, W.; Chen, Z.; Schneider, K.P.; Lasseter, R.H.; Pushpak Nandanoori, S.; Tuffner, F.K.; Kundu, S. A Comparative Study of Two Widely Used Grid-Forming Droop Controls on Microgrid Small-Signal Stability. *IEEE J. Emerg. Sel. Top. Power Electron.* **2020**, *8*, 963–975. [CrossRef]

40. Paquette, A.D.; Divan, D.M. Virtual Impedance Current Limiting for Inverters in Microgrids With Synchronous Generators. *IEEE Trans. Ind. Appl.* **2015**, *51*, 1630–1638. [CrossRef]

41. Lu, X.; Wang, J.; Guerrero, J.M.; Zhao, D. Virtual-impedance-based fault current limiters for inverter dominated AC microgrids. *IEEE Trans. Smart Grid* **2018**, *9*, 1599–1612. [CrossRef]

42. Wang, X.; Li, Y.W.; Blaabjerg, F.; Loh, P.C. Virtual-Impedance-Based Control for Voltage-Source and Current-Source Converters. *IEEE Trans. Power Electron.* **2015**, *30*, 7019–7037. [CrossRef]

43. Rodriguez-Cabero, A.; Roldan-Perez, J.; Prodanovic, M. Virtual Impedance Design Considerations for Virtual Synchronous Machines in Weak Grids. *IEEE J. Emerg. Sel. Top. Power Electron.* **2020**, *8*, 1477–1489. [CrossRef]

44. Egea-Alvarez, A.; Fekriasl, S.; Hassan, F.; Gomis-Bellmunt, O. Advanced Vector Control for Voltage Source Converters Connected to Weak Grids. *IEEE Trans. Power Syst.* **2015**, *30*, 3072–3081. [CrossRef]

45. Shah, S.; Gevorgian, V. Control , Operation , and Stability Characteristics of Grid-Forming Type III Wind Turbines Preprint. In Proceedings of the 19th Wind Integration Workshop, Dublin, Ireland, 3–12 November 2020.

46. Alves, R.; Egea-Alvarez, A.; Knuppel, T. Capabilities and limitations of black start operation for system restoration from offshore wind farms. In Proceedings of the 4th International Conference on Smart Grid and Renewable Energy, SGRE 2024—Proceedings, Doha, Qatar, 8–10 January 2024; pp. 1–6. [CrossRef]

47. da Silva, F.M.F. Analysis and Simulation of Electromagnetic Transients in HVAC Cable Transmission Grids. Ph.D. Thesis, Aalborg University, Aalborg Øst, Denmark, 2011; p. 253.

48. He, L. Effects of pre-insertion resistor on energisation of MMC-HVDC stations. In Proceedings of the IEEE Power and Energy Society General Meeting, Portland, OR, USA, 5–10 August 2018; pp. 1–5. [CrossRef]

49. Miller, N.; Foote, C. Iberdrola Innovation Middle East Distributed ReStart: Non-conventional Black-Start Resources 2021.

50. Velitsikakis, K.; Engelbrecht, C.S.; Jansen, K.; Hulst, B.V. Challenges and Mitigations for the Energisation of Large Offshore Grids in the Netherlands. In Proceedings of the International Conference on Power System Transients, Perpignan, France, 17–20 June 2019.

51. Khalilnezhad, H. Technical Performance of EHV Power Transmission Systems with Long Underground Cables. Ph.D. Thesis, TUDelft, Delft, The Netherlands, 2018. [CrossRef]

52. Khatib, A.R.; Paul, T.G.; Al-Ghamdi, S.A.; Kumar, V. Shunt Reactor Control Performances for HVAC Submarine Cable. *IEEE Trans. Ind. Appl.* **2024**, *60*, 5211–5220. [CrossRef]

53. Abeynayake, G.; Cipcigan, L.; Ding, X. Black Start Capability from Large Industrial Consumers. *Energies* **2022**, *15*, 7262. [CrossRef]

54. Lafaia, I.; de Barros, M.T.C.; Mahseredjian, J.; Ametani, A.; Kocar, I.; Fillion, Y. Surge and energization tests and modeling on a 225 kV HVAC cable. *Electr. Power Syst. Res.* **2018**, *160*, 273–281. [CrossRef]

55. Pan, Y.; Yin, X.; Zhang, Z.; Liu, B.; Wang, M.; Yin, X. Three-Phase Transformer Inrush Current Reduction Strategy Based on Prefluxing and Controlled Switching. *IEEE Access* **2021**, *9*, 38961–38978. [CrossRef]

56. Mitra, J.; Xu, X.; Benidris, M. Reduction of Three-Phase Transformer Inrush Currents Using Controlled Switching. *IEEE Trans. Ind. Appl.* **2020**, *56*, 890–897. [CrossRef]

57. Alassi, A.; Ahmed, K.H.; Egea-Alvarez, A.; Foote, C. Transformer Inrush Current Mitigation Techniques for Grid-Forming Inverters Dominated Grids. *IEEE Trans. Power Deliv.* **2023**, *38*, 1610–1620. [CrossRef]

58. Alassi, A.; Ahmed, K.; Egea-Alvarez, A.; Ellabban, O. Performance Evaluation of Four Grid-Forming Control Techniques with Soft Black-Start Capabilities. In Proceedings of the 9th International Conference on Renewable Energy Research and Applications, ICRERA 2020, Glasgow, UK, 27–30 September 2020; pp. 221–226. [CrossRef]

59. Alassi, A.; Foote, C. Modified Grid-forming Converter Control for Black-Start and Grid-Synchronization Applications. In Proceedings of the 2021 56th International Universities Power Engineering Conference, Middlesbrough, UK, 31 August–3 September 2021.

60. Seiler, P.; Packard, A.; Gahinet, P. An Introduction to Disk Margins [Lecture Notes]. *IEEE Control Syst.* **2020**, *40*, 78–95. [CrossRef]

61. Henderson, C.; Egea-Alvarez, A.; Fekriasl, S.; Knueppel, T.; Amico, G.; Xu, L. The Effect of Grid-Connected Converter Control Topology on the Diagonal Dominance of Converter Output Impedance. *IEEE Open Access J. Power Energy* **2023**, *10*, 617–628. [CrossRef]

62. Henderson, C.; Egea-Alvarez, A.; Xu, L. Analysis of optimal grid-forming converter penetration in AC connected offshore wind farms. *Int. J. Electr. Power Energy Syst.* **2024**, *157*, 109851. [CrossRef]